International Scientific-Technical and Production Journal

The Paton WELDING JOURNAL

September 2003 # 9

English translation of the monthly «Avtomaticheskaya Svarka» (Automatic Welding) journal published in Russian since 1948

Founders: *The E.O. Paton Electric Welding Institute of the NAS of Ukraine International Association «Welding»* **Publisher:** *International Association «Welding»*

Address:
E.O. Paton Electric Welding Institute,
International Association «Welding»,
11, Bozhenko str., 03680, Kyiv, Ukraine
Tel.: (38044) 227 67 57
Fax: (38044) 268 04 86
E-mail: journal@paton.kiev.ua
http://www.nas.gov.ua/pwj

State Registration Certificate
KV 4790 of 09.01.2001

Subscriptions:
$460, 12 issues per year,
postage and packaging included.
Back issues available.

CONTENTS

ALLOWANCE FOR EFFECT OF CYCLE ASYMMETRY ON CYCLIC CRACK RESISTANCE OF MATERIALS AND WELDED JOINTS

V.S. KOVALCHUK
E.O. Paton Electric Welding Institute, NASU, Kyiv, Ukraine

It was established from the results of investigations of high-strength steel welded joints that increase in values of the coefficient of asymmetry from 0 to 0.5 leads to the 3–4 times increase in rate of fatigue crack propagation at the initial region of a mean-amplitude area of kinetic diagrams of fatigue fracture and has almost no effect at its final region. Based on the analysis of these and literature data, the method and analytical expressions are suggested allowing the cycle asymmetry to be taken into account within wide ranges in determination of a cyclic crack resistance using a limited number of initial parameters.

Keywords: *cyclic crack resistance, cycle asymmetry, welded joints, calculation*

At alternating loading the fatigue cracks are formed in separate elements of metal structures at a definite (sometimes very earlier) stage. Inspection of condition of bridges, ships, nuclear and heat power units, as well as other constructions showed that many of them have fatigue cracks, whose sizes exceed the allowable sizes, being regulated by the standards of control in the process of manufacture. In welded joints the fatigue cracks are usually initiated and propagated in the area of weld mating the parent metal (along the fusion line), and also in metal of weld and heat affected zone. It is due mainly to the effect of concentration of stresses and strains caused by a geometric imperfection of shapes of welded joints, residual welding stresses and heterogeneity of geometry in zones of weld mating the parent metal in the length of the welded joint.

Cyclic life of joints at the stage of fatigue crack propagation depends on definite conditions and is comparable in many cases with a life at the stage of their initiation. Therefore, the determination of survivability of metal structures, having fatigue cracks, has a great practical importance for finding the limiting sizes of cracks at which the loss in load-carrying capacity is occurred, for assignment of terms of regular works and development of measures of arresting or delay of propagating cracks that prevents timely the emergency situations, and also the catastrophic failures.

As regards to a simple cyclic loading, there are many methods and analytical expressions for determination of interrelation between the parameters of alternating stresses and rate of propagation of fatigue cracks. They, as a rule, are based on a power dependence, established by Paris [1], of rate dl/dN of a stable growth of cracks on the only parameter ΔK (the range of the coefficient of stress intensity):

$$dl/dN = C\,(\Delta K)^m, \quad (1)$$

where dl is the increment of crack length; dN is the appropriate increment of number of stress cycles; C and m are constant coefficients, defined experimentally. In addition, the effect of cycle asymmetry on fatigue fracture of structural materials is not taken into account in many cases.

To determine the cyclic crack resistance with allowance for effect of cycle asymmetry, the Forman dependence [2], obtained by substituting a critical coefficient of stress intensity K_c at static loading to the Paris formula, is most often used:

$$dl/dN = C\,(\Delta K)^m/(1-R)K_c - \Delta K.$$

In this and other expressions [3–5] the parameters C and m are the characteristics of the material and do not depend on the coefficient of cycle asymmetry R.

It is shown in separate works on the basis of static processing of experimental data that there is a correlation relation between parameters C and m. However, the comparison of expressions obtained by different researchers [5] showed that they have comparatively narrow regions of existence and are justified only for definite values of the cycle asymmetry coefficient, mentioned by the authors.

It was established earlier [6] that the absence of allowance for effect of cycle asymmetry at the initial stage of initiation of fatigue cracks can lead to multiple errors in determination of a cyclic life. There are grounds to assume that the cycle asymmetry exerts also a similar effect on the rate of propagation of the fatigue cracks. It is evident that search for new regularities, having more complete allowances for effect of cycle asymmetry of the resistance to fatigue crack propagation, is necessary for evaluating the life of metal structures.

To evaluate the effect of cycle asymmetry of cyclic crack resistance at single-frequency loading, the experimental investigation of flat large-sized 220×18 mm section specimens made from high-strength steel (σ_y = 1000 MPa) were carried out. To initiate the fatigue fracture, the initial notches in the form of a central through crack were made in the specimens. The rate of propagation of fatigue cracks was determined at axial single-frequency soft cyclic tension (coefficient of cycle asymmetry R = 0 and 0.5). To widen the range of investigations the testing

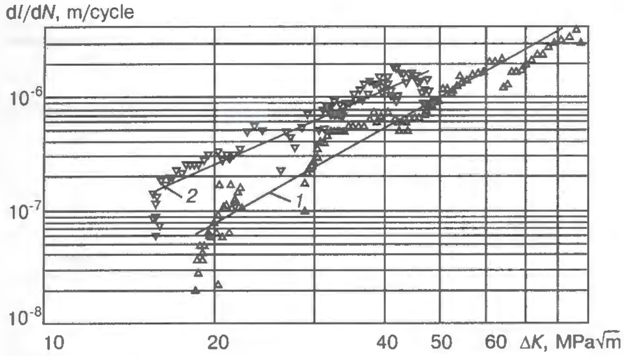

Figure 1. Diagrams of fatigue fracture of high-strength steel at from-zero (*1*) and asymmetrical (*2*) cycles of single-frequency axial tension

four specimens with different initial levels of stresses were performed at each of the mentioned R values. Specimens were cut along the rolling, the surface of plates was machined by a finishing milling, and the working part was subjected additionally to grinding. The specimens were tested in servohydraulic machine RS1 of company «Schenk» (Germany), equipped additionally with electron-optical system, providing a contact-free measurement of linear sizes of cracks at the surface of specimens within the interval from 0.1 to 200 mm at 0.01 mm accuracy.

Curves of fatigue fracture rate dl/dN–ΔK, constructed in logarithmic coordinates, are shown in Figure 1. They are approximated by expressions

$$dl/dN = 1.61\cdot 10^{-11}\,(\Delta K)^{2.82} \quad \text{at } R = 0;$$
$$dl/dN = 3.55\cdot 10^{-10}\,(\Delta K)^{2.19} \quad \text{at } R = 0.5.$$

Graphs of changing parameters C and m depending on the coefficient of cycle asymmetry R, constructed from experimental and literature data [4, 7] are given in Figure 2.

Actually, the functions $m = f(R)$ in linear coordinates R–m and function $C = f(R)$ in semi-logarithmic coordinates R–lg C have the more complex form than those shown in Figure 2. However, they can be approximated with a sufficient accuracy for an engineering practice by a broken line consisting of two lengths of straight lines which are intersected in a common point corresponding to $R = 0$.

Data of these graphs are suitable for direct allowance for effect of cycle asymmetry in determination of a cyclic crack resistance of appropriate steels at a mean-amplitude area of kinetic diagrams of the fatigue fracture or for their representation by two analytical expressions:

relative to m_R

$$m_R = m_0 + \alpha_1 R \quad \text{at } R \le 0;$$
$$m_R = m_0 + \alpha_2 R \quad \text{at } R \ge 0 \qquad (2)$$

and relative to C_R

$$C_R = 10^{\beta_1 R} C_0 \quad \text{at } R \le 0;$$
$$C_R = 10^{\beta_2 R} C_0 \quad \text{at } R \ge 0, \qquad (3)$$

where m_R, m_0 and C_R, C_0 are the parameters, respectively, at unknown and from-zero cycle asymmetry; α_1, α_2 and β_1, β_2 are the coefficients of proportionality, respectively, at $R \le 0$ and $R \ge 0$.

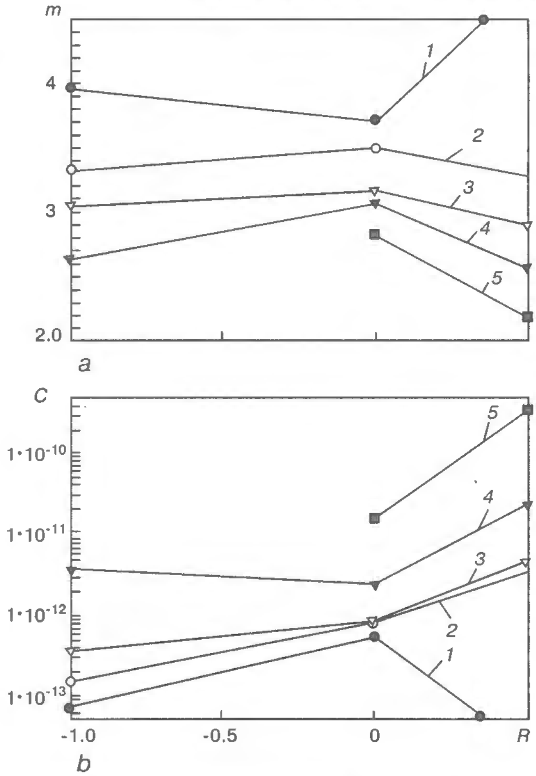

Figure 2. Dependence of parameters m (*a*) and C (*b*) on the coefficient of cycle asymmetry R: *1* — steel St3 [4]; *2* — 15KhSND [4]; *3* — 15Kh2NMFA [7]; *4* — 14Kh2GRM [4]; *5* — high-strength steel (σ_y = 1000 MPa)

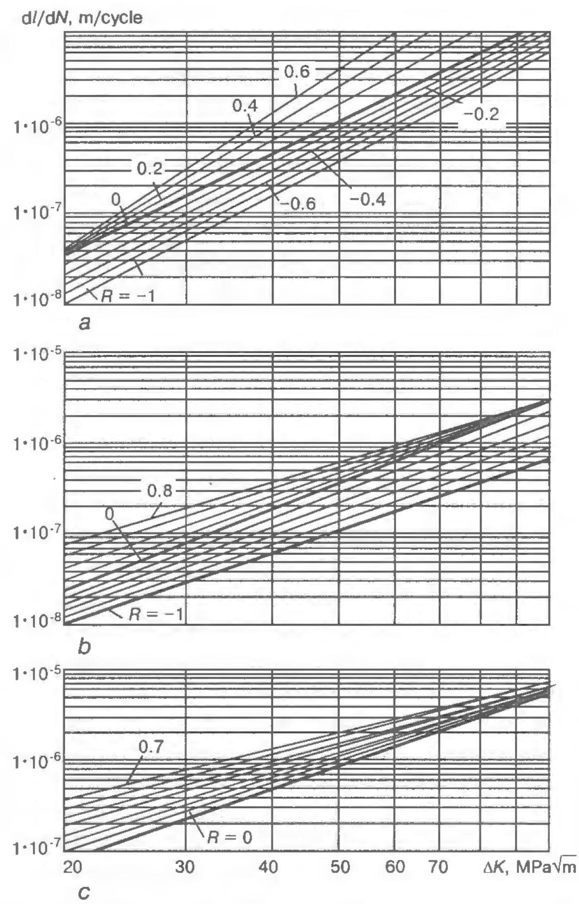

Figure 3. Calculated relationships of rate of fatigue fracture of steels at different values of the coefficient of cycle asymmetry R: *a* — steel St3 [4]; *b* — 14Kh2GRM [4]; *c* — high-strength steel

Table 1. Data for determination of cyclic crack resistance of steels at different cycle asymmetry

Steel grade	m_0	C_0	α_1	β_1	α_1	β_1
			$R \le 0$		$R \ge 0$	
St3	3.71	$5.30 \cdot 10^{-13}$	−0.25	0.86	2.23	−2.81
15KhSND	3.50	$8.10 \cdot 10^{-13}$	0.18	0.74	−0.43	1.27
15Kh2NMFA	3.16	$8.40 \cdot 10^{-13}$	0.12	0.38	−0.54	1.50
14Kh2GRM	3.07	$2.40 \cdot 10^{-12}$	0.44	−0.21	−1.00	1.99
High-strength	2.82	$1.61 \cdot 10^{-11}$	–	–	−1.26	2.69

Table 2. Results of comparison of parameters m and C at different asymmetry of cycle

Steel grade	$\gamma_{-1} = m_{-1}/\lg C_{-1}$	$\gamma_0 = m_0/\lg C_0$	$\gamma_{0.5} = m_{0.5}/\lg C_{0.5}$	$\gamma_R = m_R/\lg C_R$
St3	−0.301	−0.302	−0.339	−0.314
15KhSND	−0.259	−0.289	−0.287	−0.278
15Kh2NMFA	−0.244	−0.262	−0.255	−0.254
14Kh2GRM	−0.230	−0.264	−0.242	−0.246
High-strength	–	−0.261	−0.232	−0.247

Taking into account (2) and (3) the relationship (1) can be presented in the form

$$\begin{aligned} dl/dN &= 10^{\beta_1 R} C_0 (\Delta K)^{m_0 + \alpha_1 R} \quad \text{at } R \le 0; \\ dl/dN &= 10^{\beta_2 R} C_0 (\Delta K)^{m_0 + \alpha_2 R} \quad \text{at } R \ge 0. \end{aligned} \tag{4}$$

Numerical values of coefficients of proportionality for the above-mentioned steels at $R \le 0$ and $R \ge 0$ are given in Table 1.

The suggested approach provides more complete allowance for effect of the cycle asymmetry on cyclic crack resistance of structural materials and welded joints at simple conditions of loading.

In comparison of curves of Figure 2, *a* and *b*, constructed for a definite material, it can be concluded that there is relation between parameters m and C. It is seen from Table 2 that the average values $\gamma_R = m_R/\lg C_R = -0.31 - -0.25$ for steels of low and high strength are almost invariant to the cycle asymmetry.

Taking into account the above-described, the expression (4) takes a form

$$dl/dN = 10^{\beta R} C_0 (\Delta K)^{\gamma \lg C_0 + \alpha R} \tag{5}$$

or

$$dl/dN = 10^{\beta R m_0/\gamma} (\Delta K)^{m_0 + \alpha R}, \tag{6}$$

where the coefficients α, β and γ have indices and values, corresponding to negative or positive region of the asymmetry of loading cycle, given in Tables 1 and 2. If to neglect a low effect of coefficient of cycle asymmetry on coefficient γ, then it is possible to use the mean values γ_R in expressions (5) and (6).

To visualize the nature of changing a cyclic crack resistance under the effect of asymmetry of loading cycle, Figure 3 gives the estimated relationships, obtained from expression (4), of fatigue fracture of three grades of steels characterized by the strength. It is seen from the Figure that in case of negative values R the curves are arranged almost equidistantly, and they have a form of a fan in the region of their positive values. In addition, with increase in ΔK the intensity of growth in rate of fatigue crack propagation in steels is decreased. In kinetic diagrams of fatigue fracture, calculated from data obtained in [4] for steel St3, the fan is directed to the opposite side.

CONCLUSIONS

1. It was established experimentally that at similar values of ranges of the stress intensity coefficient ΔK the increase in values of the coefficient of cycle asymmetry from 0 to 0.5 is accompanied by 3–4 times increase in rate of growth of fatigue fracture of high-strength steel at the initial region of the mean-amplitude area of the kinetic diagrams of fatigue fracture, while at the final region this rate is remained almost unchanged.

2. The suggested method and analytical expressions make it possible to determine the cyclic crack resistance of materials and joints within the wide ranges of changes in values of the coefficient of the cycle asymmetry using a limited number of initial values of parameters m and C.

3. At the absence of the allowance for the effect of the cycle asymmetry within $-1 < R < 0.7$, the obtained values of rate of growth of the fatigue cracks in the mean-amplitude area of kinetic diagrams of fatigue fractures can ± (3–4) times differ from real values.

1. Paris, P., Erdogan, F. (1963) Critical analysis of crack propagation laws. *Tekhn. Mekhanika*, Series D, 4, 60–68.
2. Forman, R., Kerney, V., Angle, R. (1967) Numerical investigations of crack propagation in structures under cyclic loaded. In: *Transact. of American Society of Mechanical Engineers*, Series D, **3**, 8–16.
3. Troshchenko, V.T., Pokrovsky, V.V., Prokopenko, A.V. (1987) *Crack resistance of metals in cyclic loading*. Kyiv: Naukova Dumka.
4. Trufyakov, V.I., Knysh, V.V., Mikheev, P.P. et al. (1987) Dependence of fatigue crack propagation rate on asymmetry of cycle. *Avtomatich. Svarka*, **3**, 5–7.
5. Romvari, P., Tot, L., Nad, D. (1980) Analysis of laws of fatigue crack propagation in metals. *Problemy Prochnosti*, **12**, 18–28.
6. Kovalchuk, V.S. (2002) Allowance for effect of cycle asymmetry on fatigue resistance of welded joints. *The Paton Welding J.*, **4**, 24–27.
7. Troshchenko, V.T., Yasny, P.V., Pokrovsky, V.V. et al. (1981) Influence of temperature and asymmetry of loading on cyclic crack resistance of 15Kh2NMFA steel. *Problemy Prochnosti*, **10**, 3–7.

APPLICATION OF A SCANNING ELECTRON BEAM FOR WELDING TO PREVENT ROOT DEFECTS IN THICK STEELS

V.M. NESTERENKOV
E.O. Paton Electric Welding Institute, NASU, Kyiv, Ukraine

Influence was studied of disturbances of the liquid metal surface, which is on the front wall of the keyhole, on development of root defects in electron beam welding of thick steel. It is shown that a longitudinal scanning of the electron beam allows decreasing the disturbances of melt surface on the front wall of the keyhole and reducing the number of root defects in welds.

Keywords: *steels, great thickness, electron beam welding, root defects, penetration peaks, keyhole, electron beam scanning, capillary waves*

It is known [1] that root defects of the type of cold shot, developing in electron beam welding (EBW) of thick steels, are stress raisers in welds and adversely affect the mechanical properties of welded joints. Presence of root defects in the sections of crater fading out in circumferential joints, for instance in gas and steam turbine rotors, pressure vessels, stop valves, reduces the load-carrying cross-section of the joints, which is inadmissible for critical items [2]. Prevention of root defects in welded joints requires further study of the nature of their development in EBW of thick steels and determination of those parameters of the welding process, which are critical for formation of the weld root part.

The purpose of this work is determination of the influence of electron beam reflection from disturbances of the liquid metal surface on development of root defects in deep keyholes. The issue of formation of the root part of welded joints at EBW of thin and medium-thickness metals has been repeatedly raised in publications. However, no precise idea of the features of such a mechanism in welds deeper than 100 mm, was given. This is indicated by the fact that closure of circumferential butt welds and crater fading out in EBW of plate structures still is a complex task [3].

Work [4] shows that in welding with a uniformly moving electron beam the molten metal in the keyhole makes oscillations at natural frequency. The most low-frequency of the allowed modes of melt oscillation, having the maximum amplitude, prevails in this process. One of the manifestations of such oscillations are periodical splashes of the melt from the keyhole, observed during the welding process, which eventually lead to formation of structures in the form of large beads on the weld surface. This paper considers another manifestation of melt oscillations in the keyhole, namely formation of penetration peaks in the welds and the associated root defects.

The results of earlier research demonstrated that the front walls of deep keyholes in the steady-state have an inclination of 1–2° on half of the penetration depth [5]. Such small angles of incidence of the electron beam on the surface of a thin layer of molten metal affect not only the processes of metal melting and evaporation, but also the reflection of primary electrons [6], and change of the path of their motion in the keyhole. This leads to the power of the electron beam, reaching the keyhole bottom, varying in time during the welding process, the time of its variation depending on the period of natural oscillations of the melt in the keyhole. In its turn, variation of power of the electron beam, hitting the keyhole root, may cause local changes of weld depth, which is usually manifested as sharp penetration peaks of various dimensions. It is known that a rather large amplitude of variation of the penetration depth may promote formation of root defects. One of the universally accepted statements on development of root defects is the fact that defects of the type of cold shot result from a fast solidification of the molten metal before its flowing in and filling the penetrations peaks [1].

Thus, in order to reduce the probability of development of root defects in welded joints, it is necessary, on the one hand, for the amplitude of variation of the local penetration depth to be as small as possible and, on the other hand, the frequency of penetration peak appearance should be lower with the given parameters of the welding process.

It is known that in the welding process interaction of the electron beam with the front wall of the keyhole leads to the action of the recoil reaction force on the liquid metal surface, resulting from metal evaporation from the melt surface inside the keyhole [7]. In study [4] it is shown that in EBW, conducted by a uniformly moving electron beam, the recoil pressure changes only slightly in time, and melt oscillations, arising against the background of the overall motion of liquid metal over the walls of the keyhole, take place at natural frequencies. Symmetry of the problem, related to guiding the electron beam motion, results in excitation of the first mode of oscillations $m = 1$, corresponding to longitudinal displacements of the melt

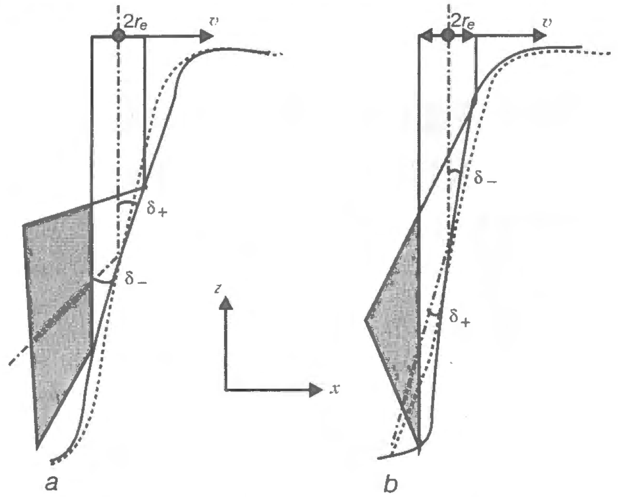

Figure 1. Increase of the effective angle of interaction of the electron beam with front wall δ_+ (*a*) and its decrease δ_- (*b*) during the welding process: r_e — radius of beam concentration; v — welding speed (dotted line shows an undisturbed surface of the melt; dashed line — the tentative zone of scattering of the central part of the electron beam)

(along the welding direction). Frequency ω_1 of the first mode of melt oscillations in the keyhole is determined according to the dispersion relationship from [4]:

$$\omega_1^2 = C_1 \frac{\sigma}{\rho} k^3, \tag{1}$$

where C_1 is the coefficient, dependent on dimensions of keyhole; σ is the coefficient of surface tension; ρ is the molten metal density; k is the wave vector of oscillations.

Let us consider the oscillations of melt surface, arising on the front wall of the keyhole. It is obvious that the lowest frequency oscillations of the melt will have the highest amplitude, their wave length being equal to approximately that of penetration depth $\lambda \approx H$ [4]. At such oscillations the effective angle of interaction of the electron beam with the melt surface on the front wall will vary during the welding process with the frequency, equal to that of natural oscillations of the melt in the keyhole. As the minimum angle of inclination of the keyhole front wall in welding of thick metal is not greater than 2°, the intensity of the electron beam, reflected from the front wall will be approximately by 1.5 times higher than at normal incidence of the beam on the metal surface [6]. With a very small angle of incidence of the electron beam on the front wall of the keyhole, even small variations of angle δ may cause considerable changes of the intensity of the reflected beam.

Figure 1 shows disturbances of melt surface in correspondence with δ_+ rise and decrease of δ_- of the effective angle of incidence of the electron beam on the front wall. The Figure shows well that with the increase of the effective angle $\delta_+ > \delta$ the reflected electrons hit the back wall of the keyhole (Figure 1, *a*), while at decrease of angle $\delta_- < \delta$ a considerable part of the electrons reaches its root (Figure 1, *b*). It is obvious that direct penetration of part of the electrons into the keyhole root leads to evolution of thermal energy on the keyhole bottom, and, therefore, also to increase of the local penetration depth. Thus, the depth of penetration varies during the welding process with a frequency, equal to that of natural oscillations of the melt in the keyhole.

Similar disturbances of the liquid metal surface in the keyhole certainly have a great influence on development of root defects, as in the first case (see Figure 1, *a*) the keyhole lower part is shielded, and in the second (see Figure 1, *b*) the greater part of energy of the reflected electron beam hits the root of the keyhole.

It is obvious that decrease of the electron beam power, reaching the keyhole root, will lead to lowering of the amplitude of penetration peaks in the weld. This may be achieved, for instance, by using a scanning electron beam, as shown in [3]. In this case, the frequency of electron beam scanning should be sufficiently high, so that the velocity of the electron beam did not affect the thermal processes, proceeding in the keyhole.

In other words, it is necessary for the electron beam not to cause any significant changes during the scanning process at temperature redistribution in the keyhole. Further on we will give the evaluation of these values.

It is known that the rate of heat propagation in a medium depends on its heat conductivity. In its turn, the rate of temperature change depends on the material diffusivity:

$$\kappa = \frac{\lambda}{\rho c},$$

where λ is the heat conductivity; c is the specific heat content of the material. For steel $\lambda = 0.8$ W/(cm·K), $\rho = 7.8$ g/cm^3 and $c = 0.44$ J/(g·K). Hence, diffusivity is $\kappa = 0.8/(7.8 \cdot 0.44) \approx 0.23$ cm^2/s. As temperature gradients along the depth of the keyhole are much smaller than those across the keyhole, the keyhole radius $R \cong 2$–3 mm may be a characteristic scale of temperature variation during the welding process. In this case the rate of propagation of temperature variations is $v_T \cong \kappa/R \cong 1$ cm/s. At the frequency of beam $f \cong 100$ Hz and amplitude $A \cong 1$ mm the scanning rate is $v_s \cong 4Af \cong 40$ cm/c. Thus, it is seen that condition $v_s >> v_T$ is satisfied with good accuracy. Therefore, by varying the frequency and amplitude of electron beam scanning it is possible to adjust the input of additional energy to the bottom of the keyhole, and, thus, affect weld formation in its root part.

Figure 2 shows the distribution of power density of electron beam, q, along welding axis x, using longitudinal scanning of the beam in the form of a symmetrical saw with amplitude $A = 0$, 1, 2 and 4 of radius r_e of beam concentration. A static electron beam, shown in Figure 2, has a Gaussian distribution of power density, where q_0 denotes full power of the beam. It is seen from the Figure that with increase

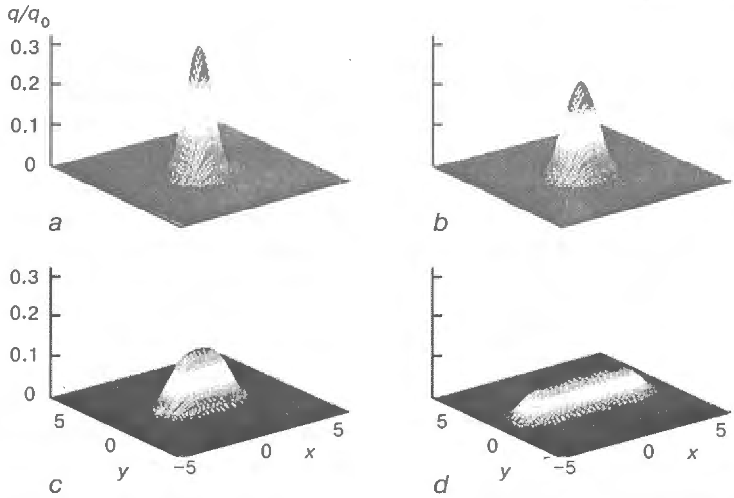

Figure 2. Distribution of power density of the electron beam q, when using the longitudinal beam scan along axis x in the form of a symmetrical saw with different amplitude of radius r_e of beam concentration: a — $A = 0$; b — $1r_e$; c — $2r_e$; d — $4r_e$

of scanning amplitude the electron beam power is redistributed along the scanning direction, and it no longer is a Gaussian beam. On the other hand, the maximum power density of the electron beam, which at $A = 4r_e$ is equal to ≈ 25 % of the maximum power of a static electron beam, is also reduced.

This leads to the conclusion that when using beam scanning the power, scattered at disturbances of the keyhole front wall, also decreases. This should inevitably lead to decrease of the amplitude of the penetration peaks in the keyhole root, which also leads to lower probability of root defect formation in welds.

However, the frequency of the used electron beam scanning cannot be too high, as at a high frequency of oscillations ($\omega/2\pi >> 1$ Hz) attenuation factor γ, averaged over a period, is given by the following dependence:

$$\gamma = 2\nu k^2 \cong \omega^{4/3},$$

where ν is the dynamic viscosity of the liquid [8]. Such a dependence provides a fast attenuation of high-frequency oscillations of the melt in the keyhole. At a low frequency of oscillations γ is mainly determined by losses near keyhole walls, which depend on frequency — $\gamma \cong \omega^{1/2}$ [8]. Substituting formula (1) into this equation, we may obtain the following dependence of attenuation coefficient γ on wave vector of oscillation k for the first mode of low-frequency oscillations of the melt in the keyhole:

$$\gamma(k) \cong \omega^{1/2} \cong (C_1(k)\, k^3)^{1/4}, \quad (2)$$

where coefficient C_1 is determined by a formula from [4]:

$$C_1(k) = \frac{[K_1'(kR)I_1'(kR_2) - I_1'(kR)K_1'(kR_2)]}{[I_1'(kR)K_1'(kR_2) - K_1'(kR)I_1'(kR_2)]}, \quad (3)$$

where I_1 and K_1 are modified Bessel functions of the 1st and 2nd kind, respectively; I_1' and K_1' are the derivatives from these functions, respectively; R and R_2 are the inner and outer radii of the keyhole, respectively.

As in the long wavelength region of the spectrum of melt oscillations in the keyhole ($k < 1/R$) coefficient C_1 is inversely proportional to wave vector $C_1 < k^{-1}$ [4], we may come to the conclusion that at a low attenuation frequency γ depends on k much less ($\gamma \cong k^{1/2}$) than at a high frequency, when $\gamma \cong k^2$.

One of the key factors, influencing the hydrodynamic stability of the keyhole during the welding process, is the amplitude of oscillations of molten metal on keyhole walls. It is known [9] that oscillations excited at resonance (natural) frequencies of the system, have the highest amplitude. Near the resonance the amplitude of forced oscillations is inversely proportional to the frequency of beam scanning and attenuation $A \cong (\omega\gamma)^{-1}$.

In [4] it is shown that the spectrum of natural oscillations of the melt in the keyhole has a discrete structure, the interval between the neighbouring natural frequencies being reduced with increase of penetration depth. Let us use formulas (2) and (3) to evaluate attenuation factors γ_{Fe} and amplitude A for the first mode of iron melt oscillations for the case of keyhole of depth $H = 120$ mm with inner $R = 2$ mm and outer $R_2 = 3$ mm radii. Results of evaluation for oscillation harmonics with numbers $n = 1$–128 are given in the Table, where k_n is the wave vector of n-th harmonics of oscillations; f_n is the corresponding frequency of oscillations; ω_n is the inherent circular frequency; A_n is the oscillations amplitude, referred to that of first harmonics A_1.

As is seen from the Table, at increase of harmonics number n, and, therefore, wave vector k_n, natural oscillations frequency ω_n rises superlinearly — $\omega_n \cong n^p$ ($p > 1$). In particular, for high oscillation harmonics $n >> 1$, we have $p \cong 3/2$. In view of the fact that with increase of wave vector k attenuation factor γ increases according to formula (2) — $\gamma \cong n^{3/4}$, oscillations amplitude decreases by the exponential law $A_n \cong (\omega_n\gamma)^{-1} \cong n^{-(p + 3/4)}$, which for $n >> 1$ takes the form of $A_n \cong n^{-9/4}$. From the Table it is seen that at increase of harmonics number n 2 times, the amplitude

Parameters of iron melt oscillations in the keyhole (H = = 120 mm, R = 2 mm, R_2 = 3 mm)

n	R_n, cm^{-1}	f_n, Hz	ω_n, rad/s	γ_{Fe}, s^{-1}	A_n/A_1
1	0.131	0.37	2.33	0.0003	1.0
2	0.393	1.12	7.01	0.0031	$1.9\cdot10^{-1}$
4	0.916	2.66	16.7	0.0168	$5.1\cdot10^{-2}$
8	1.964	6.14	38.6	0.0771	$1.4\cdot10^{-2}$
16	4.058	15.80	99.4	0.3293	$3.2\cdot10^{-3}$
32	8.247	47.60	299.0	1.3602	$5.4\cdot10^{-4}$
64	16.620	145.00	910.0	5.5273	$7.9\cdot10^{-5}$
128	33.380	409.00	2569.0	22.2840	$1.1\cdot10^{-5}$

of forced oscillations decreases $2^{9/4} \cong 5$ times in the given frequency range.

As was noted above, the spectrum of natural oscillations of the melt in the keyhole is discrete, and the density of the spectrum decreases with increase of frequency. Thus, according to formula (1), for a keyhole of depth H = 120 mm, the distance between neighbouring natural frequencies, equal to 1 Hz, is $\Delta\omega/2\pi < 1$ Hz, and at the frequency of 512 Hz it is $\Delta\omega/2\pi \cong 6$ Hz. The high density of the spectrum of melt oscillations in deep keyholes ($H \geq 80$ mm) enables resonance excitation of the natural frequency, when using the electron beam scan in the subhertz and hertz ($f \leq 10$ Hz) ranges, where the attenuation is small — $\gamma << 1$ (see the Table). Resonance oscillations of the melt in the keyhole are manifested in the experiments in the form of liquid metal spattering from the keyhole in EBW with scanning electron beam. It is obvious that such resonance phenomena adversely affect the weld quality, and they should be avoided in selection of the frequency of electron beam

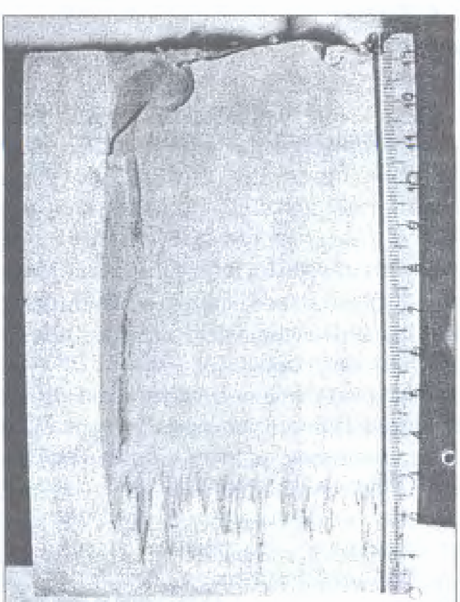

Figure 3. Longitudinal macrosection of a sample of low-alloyed steel 12CrMoV made by an electron beam moving regularly at velocity v = 5 mm/s (penetration peaks and root defects are visible in the weld lower part)

scanning. This may be achieved by applying a scanning electron beam at higher frequencies (f > 100 Hz), where attenuation already becomes essential — $\gamma > 1$.

Thus, in welding thick metals use of a longitudinal scan of the electron beam at frequencies above a certain limit value f_{lim}, does not seem to be rational, as at frequencies $f > f_{lim}$ the magnitude of the amplitude of forced oscillations will be negligibly small (see the Table), and the influence of electron beam scanning on the oscillatory processes in the keyhole will be insignificant. In EBW of low-alloyed steels 100 mm thick and more, the upper level of frequency is $f_{lim} \cong$ $\cong 200$ Hz. Therefore, the optimum frequency of electron beam scanning in welding of thick steel should be in the frequency range f = 100–200 Hz.

Figure 3 shows the oscillations of penetration depth in low-alloyed steel 12CrMoV as sharp peaks of various depth in EBW with an electron beam of velocity v = 5 mm/s. Beam power was P = 42 kW (U = 60 kV, I = 0.7 A). In order to study the shape of the keyhole front wall, the sample was not welded along its entire length (for this purpose the electron beam was quickly switched off for 1 ms). In the Figure traces of molten metal flowing in are readily seen in the upper part of penetration peaks, and root defects as dark cavities of various dimensions are visible in its lower part.

The frequency of penetration peaks, shown in Figure 3, may be determined, knowing the welding speeds. In [4] it is shown that the spectrum of natural oscillations of liquid metal in the keyhole is discrete. Therefore, melt oscillations may proceed not at one, but at several frequencies. Of all the frequencies of natural oscillations of the melt, the lowest allowed frequency (first harmonics) will have the highest amplitude, where the values are determined by formula (1). However, it is possible that scattering of the electron beam on the next higher frequency of the second harmonics, will also contribute to formation of penetration peaks. Therefore, as the second harmonics has a lower amplitude, the penetration peaks related to it, will also have a smaller depth. In its turn, higher harmonics may be disregarded, as the amplitude of natural oscillations of the melt drops in inverse proportion to the frequency and coefficient of attenuation, $A \cong 1/(\gamma\omega)$, which for the third harmonics equals values, smaller by an order of magnitude than the amplitude of the first harmonics $A_1/A_3 \cong 11$.

Let us perform Fourier analysis of penetration peaks, shown in Figure 3. For this purpose, it is convenient to use a standard mathematical procedure of fast discrete Fourier transform. Figure 4 gives the results of Fourier analysis of penetration peaks as a dependence of the square of the Fourier image amplitude on frequency. Such a dependence is convenient in that it gives an idea of the intensity of the analyzed process. From the Figure it is seen that the subhertz region of the spectrum has several high-intensity peaks. Of all the peaks of Fourier image, shown in

Figure 4, a wide peak of the maximum amplitude is notable, the position of which corresponds to the frequency $f_{max} \cong 0.74$ Hz. This means that the main scattering of electron beam power proceeded exactly on this frequency.

In view of the above-said, it is of interest to compare the frequency of formation of peaks of the penetration depth (Figure 3) with a theoretical value of the least natural frequency f_1 of melt oscillations in the keyhole:

$$f_1 = \frac{\omega_1}{2\pi} = \frac{1}{2\pi}\sqrt{C_1\frac{\sigma}{\rho}k^3}.$$

Here coefficient C_1 is found from formula (3).

For calculation of C_1 it is necessary to know the values of penetration depth H, as well as inner R and outer R_2 radii of the keyhole. R_2 and H values can be determined rather accurately by a macrosection of a welded sample. In view of the fact that direct measurement of the inner radius of the keyhole is rather difficult to perform in practice, R value will be used as a varied parameter in f_1 calculation. For a sample of low-alloyed steel 12CrMoV, shown in Figure 3, using weld macrosections it was established that the average penetration depth was equal to $H \cong 110$ mm, and the value of outer radius at half the penetration depth was $R_2 \cong 2$ mm. As at small values of dimensionless parameter kR ($kR << 1$) value of C_1 coefficient decreases in inverse proportion to kR, and the inner radius of the keyhole cannot exceed the concentration radius r_e of the electron beam, the upper estimate of frequency f_1 of the first harmonics of natural oscillations of the melt can be derived. As radius r_e of electron beam concentration was ≈ 0.5 mm in this experiment, and the wave vector of the first harmonics of melt oscillations was $k = \pi/2H \approx 0.14$ cm^{-1}, the value of kR parameter should exceed $7\cdot10^{-3}$($kR \geq 7\cdot10^{-3}$). In this case coefficient $C_1 < 129$, therefore, frequency f_1 should not exceed 1.25 Hz:

$$f_1 \leq \frac{1}{2\pi}\sqrt{129\frac{12000}{7.3}\left(\frac{\pi}{2\cdot11}\right)^3} \cong 1.25\ [\text{Hz}]. \quad (4)$$

Evidently, the value of the frequency of penetration peaks formation, derived experimentally, does not exceed evaluation by formula (4) — $f_{max} \cong 0.74f_1 < 1.25$ Hz. A good agreement between the calculation and experimental data is achieved at inner radius of keyhole $R \cong 1$ mm. In this case, the value of the frequency of the first harmonics of natural oscillations of the melt in the keyhole will be $f_1 \approx 0.73$ Hz, which practically coincides with the frequency of oscillation of penetration depth $f_{max} \cong 0.74$ Hz.

Figure 5 shows a macrosection of a steel sample, made at the same parameters as a sample in Figure 3, but already with application of a longitudinal beam scan in the form of a symmetrical saw with the frequency $f = 133$ Hz and amplitude $A = 3$ mm. Welding speed, as in the previous case, was equal to 5 mm/s.

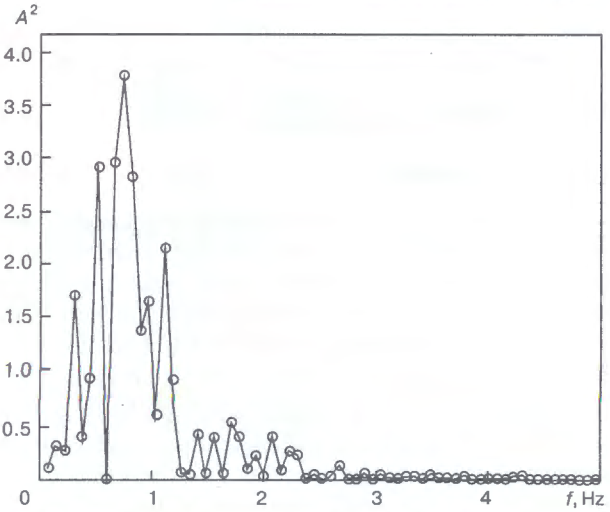

Figure 4. Frequency distribution of the square of amplitude of penetration peak Fourier images shown in Figure 1

Under such conditions oscillations of the penetration depth have a much smaller amplitude, compared to welding by a static beam. The radius of the electron beam in the focal plane is equal to approximately $r_e \cong 0.5$ mm, which corresponds to scanning amplitude $A \cong 6r_e$. This means that in this case the peak power of the beam dropped approximately 6 times, compared to the static beam (see Figure 3), which fully corresponds to reduction of the amplitude of penetration peaks in Figure 5. In addition, it is seen from the Figure that in EBW with application of electron beam scanning, the number of root defects decreased significantly. This leads to the conclusion about the rationality of application of a scanning electron beam in the frequency range of $f = 100$–200 Hz to eliminate root defects in welding thick steels.

It is clear that the exact value of the frequency of electron beam scanning will depend on penetration

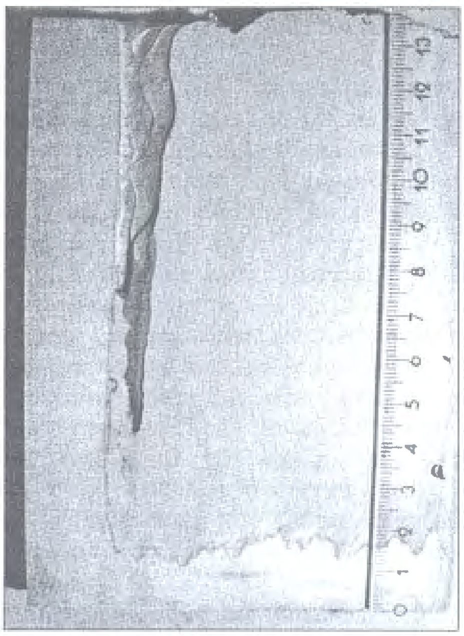

Figure 5. Longitudinal macrosection of a sample of low-alloyed steel 12CrMoV obtained at application of a longitudinal scan of the electron beam at $f = 133$ Hz and $A = 3$ mm (root defects are absent in the weld)

depth, and should be separately selected for a keyhole of a particular depth. In this experiment at welding speed of 5 mm/s the optimum value of frequency for a keyhole 120 mm deep was $f = 133$ Hz.

CONCLUSIONS

1. One of the factors, influencing development of root defects, is reflection of the electron beam from an oscillating surface of liquid metal, which is on the keyhole front wall. Such melt oscillations lead to the power of electron beam, reaching the bottom of the keyhole, changing during the welding process, which results in formation of penetration peaks in welded joints. Analysis of the amplitude of penetration peaks showed a god fit of the frequency of their appearance in welds with the least frequency of natural oscillations of the melt in the keyhole. It is established that because of a small amplitude, the higher harmonics ($n > 2$) of natural oscillations of the melt have no influence on the magnitude of penetration peaks (and, hence, on root defect formation).

2. Application of a longitudinal (along the welding direction) scanning of the electron beam in the form of a symmetrical saw in the frequency range $f = 100$–200 Hz allows achieving a lowering of disturbances of melt surface on the keyhole front wall, and, as a result, an essential lowering of the amplitude of penetration peaks and number of root defects in welds 120 mm deep, produced in EBW of low-alloyed steels at the welding speed of 5 mm/s. Available theoretical results agree well with the experimental data.

1. Paton, B.E., Leskov, G.I., Zhivago, L.I. (1976) Specific features of weld formation in electron beam welding. *Avtomatich. Svarka*, **3**, 1–5.
2. Gejkin, V.A., Puzanov, S.G. (1997) Electron beam welding of refractory titanium and nickel alloys. *Materialovedenie*, **6/7**, 46–47.
3. Dilthey, U., Dobner, M. (1993) Elektronenstrahlschweissen von radialen Ringnahten an Bauteile grossen Wanddicke. In: *Schweissen und Schneiden'93*. Duesseldorf: DVS.
4. Nesterenkov, V.M. (2003) Special features of capillary waves in the vapour-gas channel in electron beam welding of thick metal. *The Paton Welding J.*, **4**, 7–12.
5. Nesterenkov, V.M. (1989) *Investigation and development of methods of weld pool stabilisation and weld quality improvement in electron beam welding*. Synopsis of Thesis for Cand. Techn. Sci. Degree. Kyiv: PWI.
6. Pinsker, Z.G. (1976) *Electron diffraction*. Moscow: AN SSSR.
7. Leskov, G.I., Trunov, E.N., Zhivago, L.I. (1976) Shape, sizes and stability of vapour-dynamic channels in electron beam welding metal. *Avtomatich. Svarka*, **6**, 13–17.
8. Landau, L.D., Lifshits, E.M. (1986) *Hydrodynamics*. Moscow: Nauka.
9. Landau, L.D., Lifshits, E.M. (1988) *Mechanics*. Moscow: Nauka.

ASSESSMENT OF TECHNOLOGICAL STRENGTH OF PLATE HARDENABLE STEEL JOINTS WITH MULTILAYER WELDS

A.T. NAZARCHUK, V.V. SNISAR and **Yu.A. ZABURANNY**
E.O. Paton Electric Welding Institute, NASU, Kyiv, Ukraine

Peculiarities in the development of a new approach to assessment of technological strength of hardenable steel joints with multilayer welds are considered. On their basis the feasibility of application of a method of composite specimens for assessment of not only weld metal, but also welded joint as a whole, has been substantiated and confirmed experimentally.

Keywords: *hardenable steels, technological strength, cold cracks, test methods, instrument methods, technological samples*

The solution of problems of quality of welding hardenable steels is connected indispensably with a search for methods of improving technological strength because of a susceptibility of welded joints made from the above-mentioned steels to the crack formation. The most difficult task is the prevention of cold crack formation [1–4]. Today, there is no acceptable solution, in particular for welding high-strength hardenable steels with welds equal in strength to the parent metal.

Traditionally, to assess the technological strength of hardenable steel joints, the quantitative (using instruments) and qualitative (using technological samples) methods of tests are used. Their advantages and drawbacks are well known [1–4]. When the quantitative methods of testing joints with multilayer welds are used, it is necessary to take into account some peculiar features. They are connected, first of all, with an increased susceptibility of joints to the formation of transverse cold cracks. The attention was paid long ago on the hazard of their formation in welded joints with multilayer welds [1, 2].

Over the many years a lot of data has been accumulated on an integrated assessment of technological strength of hardenable steel welded joints using qualitative and quantitative methods of tests [1–3, 5]. Formerly, a special attention was paid to a hardening hypothesis of cold crack formation, and also to the negative effect of hydrogen on the formation of these cracks (hydrogen hypothesis) [1–4].

Recently, different aspects of effect of hardening phenomena are also studied [6–10], the new data are appeared about the hydrogen distribution in welded joints and its importance in the formation of cold cracks, about the role of temperature at hydrogen-induced cracking of steels and welded joints [11–13]. Problems of preheating and postweld heating are widely analyzed with allowance for hydrogen content in welding high-strength steels, peculiarities of forming structures, rate of deformation.

Taking into account the role of hardening phenomena and exclusive importance of hydrogen effect on technological strength of the joints [14–16], we have made an attempt on the basis of the analysis of testing the welded joints with multilayer welds to develop the integrated approach to the assessment of technological strength of joints with these welds in welding plate hardenable steels.

The principle of this approach is as follows. The test methods used should provide an objective integrated estimate of welded joints resistance against both longitudinal and also transverse cold cracks. The joints of hardenable steels with multilayer welds have different resistance to these cracks. However, the most complex task in this case is the prevention of formation of transverse cold cracks. It was established experimentally [15] that in producing welded joints, resistant to transverse cold cracks, a sufficient resistance also to longitudinal cracks is guaranteed, the reverse relation is not being observed.

Most of quantitative methods do not indicate for what kinds of cold cracks (longitudinal or transverse) the resistance is evaluated. The qualitative test methods (technological samples) allow us to assess the resistance of welded joints both against the longitudinal and also transverse cold cracks. Taking into account the advantages and drawbacks of technological samples it should be noted that their application (due to high labour-intensity) is rational at the final stage of investigations.

When using the quantitative methods for assessment of resistance of welded joints against cracks, those methods are preferable, which evaluate not only the resistance against the definite cold cracks (longitudinal or transverse), but account also to a great extent for effect of change in stresses during welding as a result of interaction of temporary stresses, stipulated by changes in metal volume by heating and phase transformations. In this connection, the attention should be paid to the fact that longitudinal cracks are formed under the dominating action of transverse stresses and the transverse cracks are formed under the dominating action of longitudinal cracks [1], therefore, it is rational to consider all the quantitative

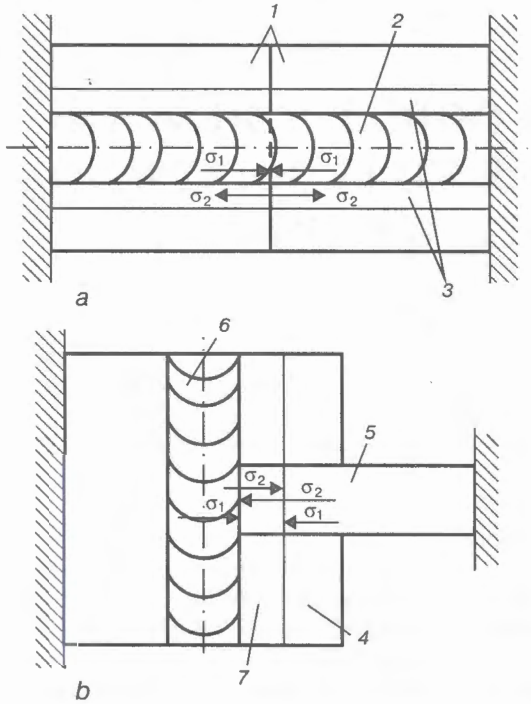

Figure 1. Scheme of interaction of temporary tensile σ_1 and compressive σ_2 stresses in the zone of welding: *a* — composite specimen, in HAZ metal of which the phase transformations take place with increase in volume (*1* — composite specimens; *2* — weld; *3* — HAZ); *b* — specimen-insert (*4, 5* — rigidly fixed specimen and insert, respectively; *6* — weld; *7* — HAZ)

methods, providing transverse loading of specimens, as tests only for longitudinal cold cracks. This remark is correlated completely with data on welding steels 14KhN4MDA and 30Kh2N2M, when appropriate tests using quantitative methods showed a sufficient resistance of these joints against longitudinal cracks at low their resistance against transverse cracks [15].

Procedure was selected and updated for testing transverse cold cracks, providing the use of a longitudinal loading of test composite specimens welded with a multilayer weld normal to surface of their contacting [14, 15, 17]. The analysis of assessment of resistance of welded joints against cold crack resistance from the results of a phase change of metal volume in weld zone [16] of both longitudinal and also transverse cracks contributed to the improvement of this procedure.

With increase in metal volume (for example, in welding composite specimens for transverse crack tests) the compressive stresses in HAZ are growing (metal volume increase is observed) and at the same time (due to phase transformations) the tensile stresses in volumes of weld metal which contact the HAZ metal are increased (Figure 1, *a*). When testing using the implant method (Figure 1, *b*), the decrease in tensile stresses will be observed as a result of increasing the metal volume in HAZ (if the phase transformations in it are proceeding with a volume increase).

The above-described circumstances allow us to use the offered procedure for assessment of not only the weld metal, but also (though indirectly) of the welded joint as a whole in welding hardenable steels, when the increase in volume of metal in phase transformations is observed in HAZ metal. The offered procedure takes into account the effect of weld metal on HAZ and effect of HAZ metal on weld, and it is the mutual effect that takes place in real welded joints (moreover, to assess joints with multilayer welds it is recommended to make them with four-five layers).

Results, obtained by using a selected quantitative method, should have a clear correlation with results, obtained in investigation of rigid large-sized samples.

The earlier works [15] were carried out for establishing the correlation of results of test for a delayed fracture (using the above-mentioned updated procedure) with results of assessment of formation of longitudinal and transverse cracks using large-sized rigid technological samples of Central R&D Institute of Shipbuilding Technology (TsNIITS) type in welding 14KhN4MDA and 30Kh2N2M steels of 40 and 80 mm thickness, respectively.

The integrated assessment of the technological strength of joints was used in the development of the

Table 1. Technological characteristics of welding process

Steel grade	*Thickness, mm*	*Size of sample or product, mm, mass, kg*	*Welding wire grade*	*Characteristics of welding process optimizing*					
				Single-arc			*Two-arc*		
				Length of area of autopreheating, mm	*Heat input, kJ/cm*	*Temperature of autopreheating, °C*	*Distance between arcs, mm*	*Heat input, kJ/cm*	*Temperature of autopreheating, °C*
14KhN4MDA	40	TsNIITS sample 1200×1600, 585	Sv-07KhGSN3MD	250–275 2 layers per pass	24–25	220–230	250–275	24.5–25.5	220–230
30Kh2N2M	80	TsNIITS sample 1200×1600, 1170	Sv-07KhGSN3MD	265–285 3 layers per pass	26.0–28.5	250–275	265–285	26.0–28.5	250–275
34KhN3M + St3	100 + 30	Gear wheel of 1800, 2200 dia., up to 8000	Sv-08G2S	–	–	–	275–325	≈ 40.0	300–320

Table 2. Dependence of coefficient of a delayed fracture $K_{d.f}$ of characteristics of the welding process

Steel grade	*Method of welding*	*Welding wire*	*Delayed fracture* σ_{cr}, *MPa*	*Yield strength of weld metal* σ_{WM}, *MPa*	$K_{d.f} = \frac{\sigma_{cr}}{\sigma_{WM}}$
14KhN4MDA	Two-arc welding	Sv-10GN2SMD	612–580	681–697	0.89–0.83
	Single-arc welding, two layers per pass		575–555	710–712	0.80–0.78
30Kh2N2M	Same	Sv-10KhG2SMA	275–255	780–796	0.35–0.32
	Single-arc welding, one layer per pass		0*	798–820	0
35KhN3M + St3	Two-arc welding	Sv-08G2S	330–320	367–374	0.89–0.85

*After making five layers the fracture of welded specimens from steel 30Kh2N2M was observed without applying external load.

technology of welding hardenable steels of different thickness (Table 1) for manufacture of bodies [15] and large-sized gear wheels of up to 8 t mass.

Technology of consumable electrode CO_2 welding of hardenable steels using welds, similar to parent metal, without preheating was developed. The content of diffusive-mobile hydrogen in deposited metal, determined by the method of alcohol sample, did not exceed 1.5 cm^3 per 100 g of metal. The autopreheating was used for prevention of cold cracks. The selection of parameters of the welding process was made so that to provide temperature of autopreheating of metal in the zone of welding at a definite distance from arc, at which it is possible to prevent the cold crack formation. The basic characteristics of the process optimizing using single- and two-arc welding are given in Table 1. To provide the necessary technological strength and required mechanical properties of joints the optimization of condition parameters and characteristics of autopreheating was realized using two-arc welding or fulfillment of the welding process by a single arc using scheme «two or three layers per one pass». Using optimizing of a single-arc welding by scheme «one layer per one pass», the reduction of mechanical properties of the joints due to increase in duration of metal holding at temperatures above A_{c_3} is possible.

The results of multiple experiments (Table 2) showed that in producing ratio σ_{cr}/σ_{WM} = 0.7–0.9 (σ_{cr} – index of assessment for a delayed fracture during 24 h using method of composite specimens; σ_{WM} – yield strength of high-strength weld metal, similar to parent metal) the welded joints resistant to longitudinal and transverse cold cracks are guaranteed in principle. The feasibility of use of characteristic, similar to σ_{cr}/σ_{WM}, was also mentioned in [18], however, the authors have another opinion as to a limiting value of this ratio.

The use of other methods, using instruments, for assessment of welded joints with multilayer welds (for example, implant method with different variants of improvement, classical test for a delayed fracture [1, 2]) does not guarantee the necessary correlation regarding the assessment of resistance to transverse and longitudinal cracks of joints with multilayer welds. Thus, for example, in welding of sample of TsNIITS type of 1200×1600 mm (steel 30Kh2N2M of 80 mm thickness) using the technology which provided the high resistance against the formation of longitudinal cracks, the formation of a large amount of transverse cracks occurred along the entire length of weld after 3–5 days.

There is an opinion that many instrument methods should be used for comparative tests. However, the comparative capabilities of these methods are exhausted earlier than it is necessary for obtaining the optimum variant. It was not mere a coincidence, that, for example, in use of implant method the attempts were made of its improvement using a circular boring or threaded cutting of specimens, etc.

It should be noted that producing thermal and deformational cycles, close to corresponding cycles of welding real joints, is provided in use of the offered procedure of composite specimens. Here, there are no problems with loading of specimens even of large sizes as, actually, only the weld metal is subjected to loading independently of a size of specimens.

Assessment of susceptibility to crack formation in accordance with [16] is rational by a sum of two or three components of stresses in rigidly fixed specimen or insert. They include the values of stress directly before the beginning of phase transformations, values of decrease in tensile stresses as a result of phase change in volume and values of stresses after the complete cooling of the specimen or insert [16]. In [6, 7] the characteristic $\Delta\sigma_d$ is taken as an estimate of susceptibility of welded joints to crack formation. This characteristic represents a difference between stresses acting before the beginning of phase transformations, and directly after their proceeding with allowance for the temperature during $\gamma \rightarrow \alpha$ transformation. The following assumption can be made on the basis of works [6, 7, 16] and results of tests for transverse cracks using the method of composite specimens [14, 15] (where the increase in tensile stresses in weld metal due to increase in volume of HAZ metal as a result of phase transformations). If to consider the real welded joint (but not an insert of rigidly fixed specimen of the limited section), the formation of tensile stresses in HAZ metal during cooling (when the de-

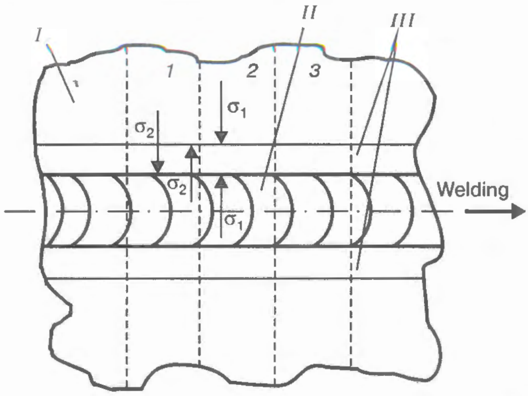

Figure 2. Scheme, illustrating the feasibility of occurrence of transverse temporary peak stresses during proceeding of transformations in HAZ metal with increase in volume: *I* — fragment of joint (divided conditionally into areas *1–3*); *II* — weld; *III* — HAZ metal; σ_1 and σ_2 — tensile and compressive stresses, respectively

crease in metal volume and then its increase at $\gamma \rightarrow \alpha$ transformation is occurred) can lead to the appearance of temporary peak stresses.

A scheme of the joint fragment with a conditional its dividing into composed areas can serve as an example (Figure 2). If to consider areas *1* and *2* separately (when the transformation occurs at the first area with increase in volume, and it has not yet occurred at the second area), then the short-time peak stresses will occur at its conditional butt. Their level will be determined by the sum of two components: stresses, acting directly before the beginning of phase transformation, and value, by which the tensile stresses are decreased as a result of a phase increase of volume of metal of the specimen of the limited section. During transformation proceeding in HAZ metal along the weld (that takes place really in welded joint), the mentioned peak stresses will be formed synchronously with a change in place of the transformation proceeding in HAZ metal.

The offered analysis of resistance of hardenable steel joints of multilayer welds against the crack formation allows us to recommend the new approach to the integrated assessment of the technological strength of welded joints. The use of the described approach can occur to be useful not only in welding with welds similar to the parent metal, but also in welding, for example, with high-alloy austenitic-martensitic welds [19].

CONCLUSIONS

1. As regards to application of the quantitative methods of tests, the integrated approach has been suggested to the assessment of technological strength of plate hardenable steel joints with multilayer welds, based on the assessment of resistance of joints against longitudinal and transverse cracks with allowance for interaction of stresses occurring in welding as a result of thermal effect and phase transformations. The presented grounds are confirmed by data obtained in investigation of rigid large-sized samples.

2. Taking into account the above-described approach, the feasibility of use of the method of composite specimens for assessment of not only weld metal, but also the welded joint as a whole has been grounded and confirmed experimentally, as it makes possible to assess the mutual effect of weld metal on HAZ and vice versa.

3. Assumption was made that the data on mutual effect of thermal stresses and stresses caused by phase changes on metal volume in the zone of welding in study of specimens of limited sizes (of type of insert or rigidly fixed specimen) require the significant clarification in interpretation of interaction of these stresses in the real welded joints.

1. (1974) *Technology of fusion electric welding of metals and alloys*. Ed. by B.E. Paton. Moscow: Mashinostroenie.
2. Makara, A.M., Mosendz, N.A. (1971) *Welding of high-strength steels*. Kyiv: Tekhnika.
3. Makarov, E.L. (1981) *Cold cracks*. Moscow: Mashinostroenie.
4. Shorshorov, M.Kh. (1965) *Metals science of welding of steel and titanium*. Moscow: Nauka.
5. Kasatkin, S.B., Mikhoduj, L.I., Gordonny, V.G. (1996) Procedural approaches to complex investigation of delayed and brittle fracture of welded joints from high-strength low-alloy steels. *Avtomatich. Svarka*, **2**, 58–60.
6. Kasatkin, B.S., Brednev, V.I., Tsaryuk, A.K. et al. (1993) Evaluation of resistance of 15Kh2MFA steel welded joints to cold cracking. *Ibid.*, **5**, 3–7.
7. Tsaryuk, A.K., Brednev, V.I. (1998) About problem of nature of cold cracking in welding of hardenable steels. *Ibid.*, **10**, 9–13.
8. Tsaryuk, A.K., Brednev, V.I. (1996) Problems of cold crack prevention. *Ibid.*, **1**, 36–40.
9. Kasatkin, B.S., Brednev, V.I. (1985) Peculiarities of mechanism of cold crack formation in welded joints of high-strength steels. *Ibid.*, **8**, 1–6, 18.
10. Mikhoduj, L.I., Poznyakov, V.D., Yushchenko, A.K. (2000) Resistance of 12KhGN2MFDRA steel welded joints to a delayed fracture. *The Paton Welding J.*, **11**, 4–10.
11. Musiyachenko, V.F., Kasatkin, S.B. (1985) Hydrogen distribution in alloy steel welded joint and its influence on cold crack formation (Review). *Avtomatich. Svarka*, **9**, 3–8.
12. Pokhodnya, I.K., Shvachko, V.I. (1997) Physical nature of hydrogen-induced cold cracks in structural steel welded joints. *Ibid.*, **5**, 3–12.
13. Pokhodnya, I.K., Stepanyuk, S.N., Shvachko, V.I. (2000) Role of temperature in hydrogen-induced cracking of structural steels and welded joints. *The Paton Welding J.*, **2**, 2–7.
14. Nazarchuk, A.T., Sterenbogen, Yu.A., Kosyakov, V.P. (1984) Procedure of evaluation of weld metal susceptibility to longitudinal cracking. *Avtomatich. Svarka*, **12**, 7–10.
15. Nazarchuk, A.T., Sverdel, I.P. (1994) Resistance of hardenable steel joints with multilayer welds to cracking. *Ibid.*, **1**, 15–19.
16. Nazarchuk, A.T., Kosyakov, V.P. *Method of testing of hardenable steel welded joints on cold cracking susceptibility*. USSR author's cert. 1585709. Int. Cl. G 01 3/00. Publ. 15.08.90.
17. Shlepakov, V.N., Giyuk, S.P. (1987) Application of bead-on-plate slot sample for determination of influence of hydrogen on cold cracking. *Avtomatich. Svarka*, **4**, 37–39.
18. Sterenbogen, Yu.A., Bursky, G.V. (1987) Method of evaluation of resistance of high-strength steel welded joint HAZ to cold cracking. *Ibid.*, **3**, 1–5.
19. Snisar, V.V., Demchenko, E.L., Ivanchenko, E.V. (2000) Challenging technologies for high-strength steel welding without preheating and heat treatment. *The Paton Welding J.*, **11**, 37–40.

THICKNESS OF THE MOLTEN METAL INTERLAYER UNDER THE ARC IN SUBMERGED-ARC SURFACING

A.D. RAZMYSHLYAEV
Priazovsky State Technical University, Mariupol, Ukraine

Method for estimation of thickness of the molten metal interlayer during arc surfacing is suggested. Processes of melting (fusion) of refractory inserts of tungsten and tantalum by the welding arc, as well as their dissolution under the effect of the molten pool metal are considered. It is shown that removal of the molten pool metal during surfacing allows improvement of reliability of the data on thickness of the molten metal interlayer under the arc.

Keywords: *arc surfacing, welding arc, molten pool metal, latent component of the arc length, thickness of the molten metal interlayer under the arc*

Efficiency of arc welding and surfacing, as well as quality of the welds and deposited beads depend to a considerable degree upon the processes occurring in the weld pool, its shape and size. There are many factors that affect these processes, but the most important among them are the latent component of the arc length, $l_{a.l}$, and thickness of the molten metal interlayer under the arc, δ_m. They are little studied as yet, especially for the cases of submerged-arc welding and surfacing. In the melting zone (zone of base metal under the arc), these values are related to each other by the following equation:

$$l_{a.l} \approx H_p - \delta_m, \qquad (1)$$

where H_p is the depth of penetration of base metal.

The value of $l_{a.l}$ cannot be determined by calculations because of the presence of a solid front wall of the pool crater and absence of reliable data on the arc pressure during welding (surfacing) using a consumable electrode (especially by the submerged-arc method). Therefore, it is advisable that the value of δ_m be determined experimentally, and $l_{a.l}$ be calculated using equation (1).

With known procedures [1–6], the value of δ_m is determined by using refractory inserts with a melting point higher than that of the base metal. However, these procedures did not allow for the probable dissolution of these inserts by molten metal of the weld pool, which could lead to underestimation of experimental data. This assumption is based on the data generated by us earlier and published in [5] on the dependence of the value of δ_m upon the thickness of a refractory insert, δ_{Ta}, i.e. the 5 mm wide tantalum plate (Figure 1). In that case decrease in thickness of the insert was accompanied by increase in the intensity of dissolution of the insert by the molten pool metal. Dissolution of the insert was evidenced by a characteristic pointed shape of its top part and presence of the dissolved insert material around it (Figure 2). With the known procedures, the use of refractory inserts for estimation of δ_m may lead to an error. Different researchers [1–4] may have a different estimation error, but in all the cases the data on the values of δ_m are underestimated.

However, it can also be assumed (and this factor was taken into account by none of the researchers) that increase in thickness (diameter) of the inserts might lead to their incomplete melting by the welding arc, which could result in overestimation of the values of δ_m. Therefore, the processes of melting (fusion) of the inserts by the arc, as well as their dissolution by the molten pool metal, determining reliability of the experimental data on the values of δ_m, are unexplored so far.

The purpose of this study was to improve the method for experimental estimation of thickness of the molten metal interlayer under the arc, δ_m, during welding and surfacing. The method is based on the use of refractory inserts and provides for making a correction for the intensity of dissolution of an insert by the molten pool metal, allowing for the probability of the arc melting of parts of the insert extending over the level of the molten pool metal.

The processes of melting (fusion) of the inserts by the arc and their dissolution by the molten pool metal

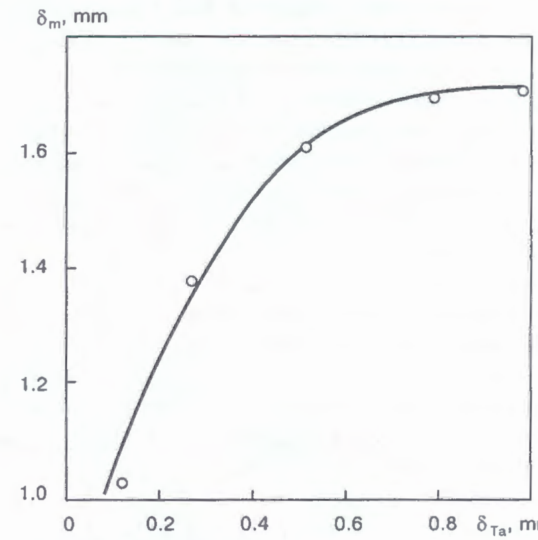

Figure 1. Thickness of the molten metal interlayer under the arc, δ_m, against thickness of the insert (tantalum plate), δ_{Ta}, in surfacing on the St3sp steel plate using wire Sv-08 with a diameter of 5 mm under the following conditions: I_s = 760–810 A, U_a = 32–33 V, v_s = 10 m/h

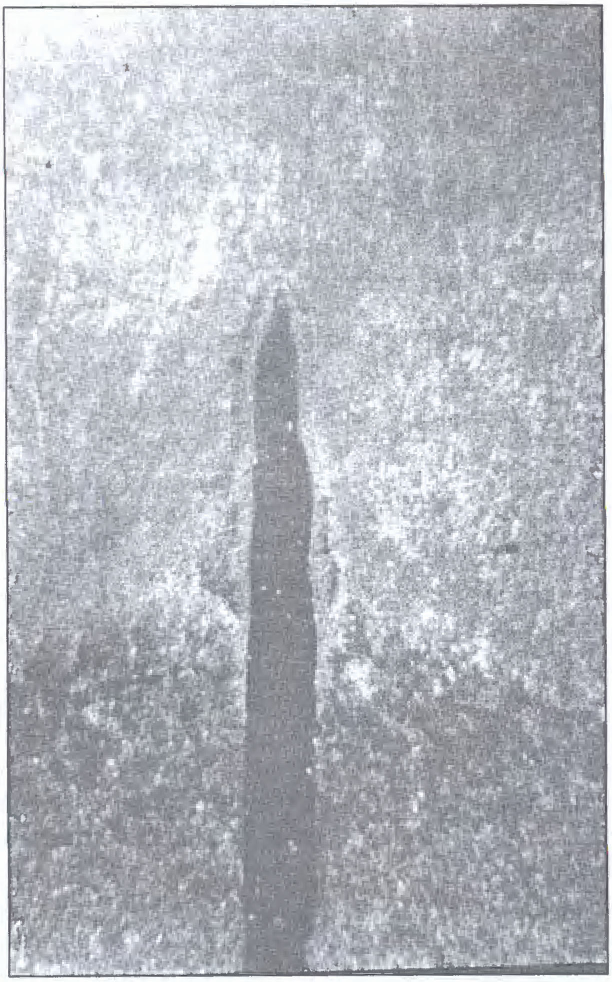

Figure 2. Macrosection of a deposited bead with refractory insert

were studied experimentally during surfacing at a direct current of reversed polarity. Like in studies [1–4], the tantalum and tungsten inserts were used for welding (surfacing) of low-carbon steels.

To study the process of melting of refractory inserts by the arc, the inserts of foil 5 mm wide and 0.25 and 0.5 mm thick, as well as wire with a diameter of 0.5 mm and rods with a diameter of 1, 1.5 and 2 mm, made from tantalum and tungsten, were placed in a butt joint between the St3sp (killed) steel plates 20 mm thick along the axis of an intended movement of the arc with a spacing of 50 mm. The inserts extended to 4 mm over the plate surfaces. The plates were installed vertically to make a horizontal joint with the inserts. The inserts were melted by the automatic open-arc welding method using the 5 mm diameter wire under the following conditions: I_w = = 700–750 A, U_a = 35–37 V and v_w = 10 and 40 m/h. Here the inserts were not dissolved by the molten pool metal. After affecting the inserts by the arc, only the tungsten rods 2 mm in diameter projected over the plate surface (crater) to 2.5 mm at v_w = 10 m/h and to 4 mm at v_w = 40 m/h. Then the experiment was repeated by decreasing the current to 400–450 A. In that case again only the tungsten rods 2 mm in diameter remained non-melted to the same length. Therefore, all of the above refractory inserts, except for the tungsten rods 2 mm in diameter, can be used for the submerged-arc welding and surfacing processes performed at a substantial welding current (400–750 A or more). Under other welding and surfacing conditions, to achieve a complete melting of the inserts by the arc, it is necessary to additionally specify their sizes.

Table 1. Mean rate of dissolution of refractory inserts, v_d, (mm/s) by the molten pool metal during CO_2 welding

Type and size of insert, mm	*Insert material*	
	Ta	*W*
Rod, diameter 2.0	0.08	–
Wire, diameter 0.5	1.20	0.50
Foil (plate)		
5×0.25	2.20	0.95
5×0.50	1.20	0.60
5×1.00	0.50	0.41

Investigations were conducted to study dissolution of tungsten and tantalum inserts by the molten pool metal during welding. For that the inserts were immersed into the tailing edge of the weld pool (down to its bottom) and moved to a distance of 15 mm from the electrode (arc) axis for a certain time period. Then welding was performed by the CO_2 method using wire Sv-08G2S 1.2 mm in diameter under the following conditions: I_w = 370–380 A, U_a = 35–37 V and v_w = = 10 m/h. In that case the tungsten insert exhibited the maximum dissolution resistance (Table 1). The mean rate of dissolution, v_d, of the tantalum inserts is about 2 times as high as that of the tungsten inserts. Shortening of the inserts has an almost linear time relationship. The rates of dissolution of refractory inserts in molten metal are approximately identical, provided that thickness of a foil (plate) is equal to diameter of a wire (rod). The rate of dissolution of the tungsten inserts 0.5 mm in diameter was approximately 0.5 mm/s.

To obtain quantitative data on dissolution of refractory inserts by the molten pool metal during submerged-arc welding (surfacing), the surfacing process using the 4 mm diameter wire Sv-08A and flux AN-348A was performed under the following conditions: I_w = 780–810 A, U_a = 28–30 V and v_s = 7.2 m/h. The refractory inserts were placed in a butt joint between the two plates of steel St3sp 20 mm thick. The inserts extended to 10 mm over the surface of the plates. Axis of the joint along which the inserts were located was at a distance of 15 mm from axis of the future bead. Because of a low arc voltage, the refractory inserts were affected only by the molten pool metal, rather than by the arc. The time of the effect by the molten pool metal on the inserts was 5–10 s, according to the calculations made with allowance for the height of the molten inserts and the

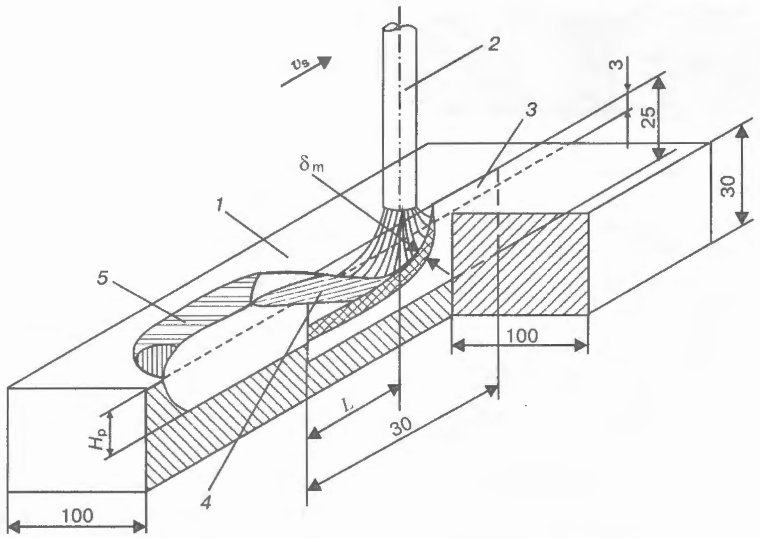

Figure 3. Schematic of a sample for measuring thickness of the molten metal interlayer under the arc during surfacing: *1* — base metal; *2* — electrode; *3* — refractory insert; *4* — molten pool metal; *5* — deposited metal

experimental data on size of the weld pool. Shortening of the inserts was counted from the top surface of the bead over an insert, as above this surface the inserts dissolved under the effect of the molten slag. As seen from the data of Table 2, the rate of dissolution of the refractory inserts during submerged-arc surfacing is not higher than during CO_2 surfacing. The mean rate of dissolution of the 0.5 mm diameter tungsten insert (as well as foil of the same thickness), v_d, is about 0.5 mm/s. Approximately the same values of v_d were obtained in using the 1 mm diameter tantalum insert and 1 mm thick foil.

As shown by the estimations, the speed of movement of the melting front deep into the base metal within depth (relative to the plate surface) ranges of 0–5, 5–10 and 10–15 mm during submerged-arc surfacing (I_w = 750–800 A, U_a = 33–35 V and v_s = = 20 m/h) is 5, 2 and 1.5 mm/s, respectively. These values are higher than the rate of dissolution of the inserts. In submerged-arc welding and surfacing using a wire, the data on thiickness of the molten metal interlayer on the front wall of the crater will be reliable, provided that the use is made of the tungsten inserts in the form of a foil 0.5 mm thick or wires 0.5 mm in diameter, as well as the tantalum inserts in the form of foil 1 mm thick or wires 1 mm in diameter. Removal (splashing out) of the molten pool metal is indicated. This makes the method for estimation of δ_m much simpler, as the crater is not filled with a solidified molten metal, and there is no need to make transverse macrosections of the deposited beads, while the size of a refractory insert in the crater can be measured.

It is suggested that refractory inserts in the form of a foil of a considerable length (e.g. 30 mm) should be used for submerged-arc welding and surfacing. Height of an insert should be larger than the metal penetration depth. With this method, the insert should be placed in a butt joint between the plates along a future bead (weld) axis. When the leading edge of the pool during the surfacing process is within the refractory insert zone (Figure 3), the molten pool metal should be splashed out, e.g. using an impact tool described in [4].

Experiments on submerged-arc surfacing using a wire showed that thickness of the molten metal interlayer on the front wall increased with deepening into the crater (Figure 4). It is characteristic also that at a steep front of melting of the insert in the leading edge of the pool, this end of the insert lowers almost rectilinearly and to an insignificant distance (to 1–1.5 mm in a region 20–25 mm long after inflection point C) (Figure 5). As shown by the calculations, shortening of the insert after the inflection point occurs at a rate equal to that of its dissolution by the molten pool metal (Table 2). To estimate the value

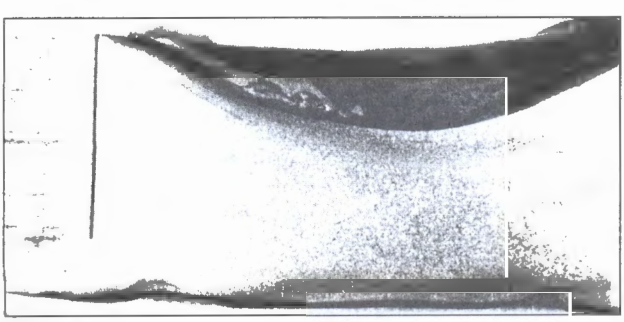

Figure 4. Macrosection of a bead deposited by using a refractory insert after splashing out of the weld pool

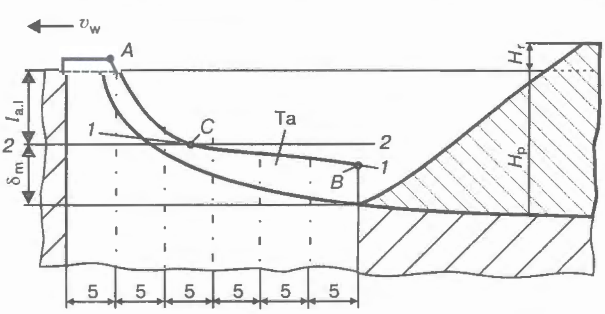

Figure 5. Diagram for estimation of the latent component of the arc length (thickness of the molten metal interlayer) in arc surfacing: ACB — insert melting line; H_r — height of reinforcement (see the rest of the designations in the text)

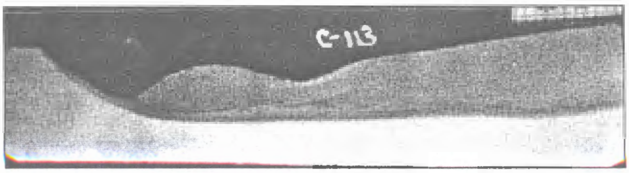

Figure 6. Appearance of the weld pool crater in a longitudinal section during submerged-arc surfacing using 4 mm diameter wire Sv-08A and flux AN-348A under the following conditions: I_s = = 680–700 A, U_a = 38–40 V and v_s = 72 m/h

of a latent component of the arc length, $l_{a.l}$, it is necessary to find the inflection point (point *C* in Fi-gure 5). As the intensity of dissolution of the insert is different with its different thickness, the angles of inclination of the end of this insert in a region located below the level of $l_{a.l}$ may also be different. To estimate $l_{a.l}$, it is necessary to draw an averaging line *1–1* up to its intersection with the end of the insert on the front wall of the crater, thus determining position of point *C*. Horizontal line *2–2* corresponds to the lowest level of location of the active arc spot on the front wall of the crater and is a latent component of the arc length, $l_{a.l}$ (see Figure 5). The distance from line *2–2* to the lowest point on the crater bottom is thickness (depth) of the molten layer, $\delta_m = H_p - l_{a.l}$.

The data on the δ_m values obtained during submerged-arc surfacing on plates of steel St3sp 20 mm thick using the 4 mm diameter wire Sv-08A and flux AN-348A are given in Table 3. Values of the latent component of the arc length, $l_{a.l}$, amount approximately to $(1/2–1/3)H_p$. Similar quantitative data were obtained also in submerged-arc surfacing using a ceramic flux of the ZhSN-1 type. It can be concluded

Table 2. Mean rate of dissolution of refractory inserts, v_d, (mm/s) by the molten pool metal during submerged-arc surfacing

Type and size of insert, mm	*Insert material*	
	Ta	*W*
Rod, diameter 2.0	0.08	0.010
Rod, diameter 1.5	0.20	0.015
Rod, diameter 1.0	0.50	0.020
Wire, diameter 0.5	1.10	0.520
Foil (plate)		
5×0.25	2.20	0.750
5×0.50	1.20	0.400
5×1.00	0.50	–
10×0.50	1.10	0.400
30×0.50	1.05	0.380

on the basis of the above data that composition of a flux has an insignificant effect on the δ_m and $l_{a.l}$ values.

To estimate the value of δ_m under the arc, it is possible to use, as shown in [1, 2], the refractory inserts of a round section (wire or rod). However, according to the method suggested, after an electrode has passed a section with the refractory insert, the molten pool metal should be splashed out. In this case it is necessary to measure distance *L* from the electrode axis (at the moment of splash of the pool) to a section with the refractory insert and the value of δ_m, as well

Table 3. Dependence of the pool crater parameters upon the surfacing conditions

Deposited bead No.	*Wire diameter, mm*	*Surfacing conditions*		*Pool crater parameters*			
		I_s, *A*	v_s, *m/h*	H_p, *mm*	$l_{a.l}$, *mm*	δ_m, *mm*	$l_{a.l}/H_p$
1	4	550–560	36	7.0	3.5	3.5	0.50
2		550–560	66	5.4	3.5	1.9	0.65
3		510–530	90	2.7	1.7	1.0	0.65
4		780–810	32	10.8	7.0	3.8	0.65
5		780–810	60	7.0	5.0	2.0	0.71
6	5	780–810	12	4.5	1.5	3.0	0.33
7		500–510	12	8.5	5.5	3.0	0.65
8		760–810	12	14.0	9.5	4.5	0.68
9		950–1000	20	6.6	4.7	1.9	0.71
10		760–810	40	5.3	3.5	1.8	0.66
11		760–810	12	6.0	1.8	4.2	0.30
12		760–810	12	13.0	11.7	1.3	0.90

Notes. 1. U_a = 33–35 V. 2. Beads Nos.11 and 12 were made by downward and upward surfacing, respectively; the angle of inclination of a plate to horizon was 8°.

as make a correction for dissolution of the refractory insert by the molten pool metal, Δ. Then thickness of the molten metal interlayer, allowing for the correction, will be as follows:

$$\delta'_m = \delta_m + \Delta = \delta_m + v_d L / v_s.$$

Data on the rate of dissolution of inserts can be taken from Tables 2 and 3.

Based on the information generated in this study on the refractory inserts melted by the arc and dissolved by the molten pool metal, it can be concluded that the data given in [6] on distribution of thickness of the molten metal interlayer on the front wall of the pool crater are underestimated, as they were obtained by using a method with which the weld pool was not splashed out and a refractory insert was dissolved by the molten pool metal.

The data presented here, showing substantial values of the latent component of the arc length, $l_{a.l}$, are qualitatively evidenced by the presence of a recess formed in the arc zone (Figure 6), where during the experimental submerged-arc surfacing an electrode was rapidly (by an impact) moved in a direction normal to the surfacing direction.

CONCLUSIONS

1. Allowance for the processes of melting of refractory inserts by the welding arc and their dissolution by the molten pool metal improved reliability of experimental data on thickness of the molten metal interlayer under the arc during submerged-arc surfacing.

2. In submerged-arc surfacing the values of the latent component of the arc length are substantial and amount approximately to $(1/2-1/3)H_p$ of base metal.

1. Chernyshov, G.G., Rybachuk, A.M. (1969) Thickness of liquid interlayer under the arc. In: *Technology and automation of welding and brazing processes*. Moscow: Mashinostroenie.
2. Kornienko, A.N., Romanenko, Ya.A. *Method for study of metal penetration process*. USSR author's cert. 1625629. Int. Cl. B 23 K 2800. Publ. 02.03.85.
3. Leshchinsky, L.K., Pavlov, I.V. (1975) Thickness of liquid interlayer under the arc in surfacing using strip electrode and wire. *Avtomatich. Svarka*, **3**, 75–76.
4. Razmyshlyaev, A.D. (1979) Investigation of speed of movement of molten metal in the weld pool during submerged-arc surfacing. *Svarochn. Proizvodstvo*, **9**, 3–5.
5. Razmyshlyaev, A.D. (1990) *Method for estimation of thickness of molten interlayer under the arc during welding*. Mariupol: UkrNIINTI.
6. Razmyshlyaev, A.D., Leshchinsky, L.K., Nesterenko, K.L. (1975) Distribution of thickness of liquid metal interlayer along the length of the weld pool crater. *Avtomatich. Svarka*, **12**, 62–63.

OPTIMIZATION OF INDUCTION HARDFACING OF THIN DISCS, ALLOWING FOR THERMAL AND ELECTROMAGNETIC SHIELDING

O.M. SHABLY[1], Ch.V. PULKA[1] and A.S. PISMENNY[2]
[1]I. Pulyuj Ternopil State Technical University, Ternopil, Ukraine
[2]E.O. Paton Electric Welding Institute, NASU, Kyiv, Ukraine

A mathematical model has been developed to determine the temperature field in the process of disc hardfacing using a two-turn ring inductor with allowance for thermal and electromagnetic shielding. This model enables optimizing the mentioned temperature in the zone of disc hardfacing depending on the parameters of the inductor, disc, electromagnetic and thermal shields, as well as electric current.

Keywords: *induction hardfacing, thin discs, two-turn ring inductor, optimizing the inductor parameters, temperature field, thermal and electromagnetic shielding, investigations, calculations*

In work [1] studies have been performed to optimize the design parameters of a two-turn ring inductor for hardfacing thin round and shaped discs of an arbitrary diameter and width of hardfacing zone, taking into account shielding of just the electromagnetic field, in order to obtain a specified power distribution over the hardfacing zone width. Dimensions of the two-turn ring inductor are selected, depending on disc diameter and hardfacing zone width, as well as allowing for the values of the coefficients of electromagnetic field shielding ($K_{sh} = 1$; $K_{sh} = 0.25$, $K_{sh} = 0$ — full shielding) [1].

It is of interest to study the temperature field in the hardfacing zone with development of a mathematical model to determine the temperature in the disc through the parameters of a two-turn ring inductor, which is used to perform heating, allowing for electromagnetic and thermal shielding simultaneously [2], which significantly affect the temperature distribution in the hardfacing zone. The developed model will allow designing the heating system (inductor, thermal and electromagnetic shields, part) for hardfacing thin round and shaped discs.

Let a round disc (Figure 1) of $2h$ thickness and r_2 radius be heated, using a two-turn ring inductor.

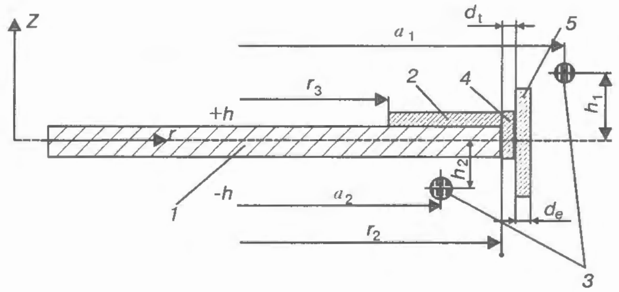

Figure 1. Cross-section of the heating system: *1* — part; *2* — charge; *3* — two-turn ring inductor; *4, 5* — thermal and electromagnetic shields, respectively

In this case the specific power of the heat sources, which emerge in the disc area under the impact of an electromagnetic field, has the form of [1]

$$w = \frac{\sigma\omega^2\mu_0^2}{128\pi^2 h} \times \\ \times [\Delta I_1^2 A^2 a_1^2 + \Delta I_2^2 a_2^2 B^2 + 4ha_1^2 I_1^2 C^2 e^{-2(r_2 - r)/\Delta}], \qquad (1)$$

where A^2, B^2, C^2 are the functions of radius r [3], geometrical dimensions of the inductor and disc h_1, h_2, $2h$, a_1, a_2, r_2 (Figure 2), as well as physical parameters of the electromagnetic field; $\Delta = \sqrt{2/(\omega\mu\sigma)}$ is the depth of penetration of the electromagnetic field into disc material (ω is the circular frequency of the electromagnetic field; μ is the magnetic permeability; σ is the electric conductivity); $\mu_0 = 4\pi\cdot 10^{-7}$ H/m.

Temperature field in the disc satisfies the equation of heat conductivity [4]:

$$\frac{\partial^2 T}{\partial r^2} + \frac{1}{r}\frac{\partial T}{\partial r} - m^2 T - \frac{1}{a}\frac{\partial T}{\partial t} = -\frac{w}{\lambda}, \quad m^2 = \frac{\alpha}{\lambda h}, \qquad (2)$$

where λ is the coefficient of heat conductivity of disc material; α is the coefficient of heat transfer to the

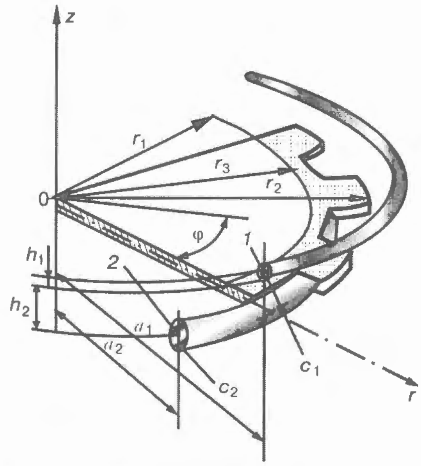

Figure 2. Schematic of a disc with the inductor: *1* — upper turn of the inductor; *2* — lower turn

environment in the absence of a shield; $T = T_1 - T_{en}$ (T_1, T_{en} are the temperature of the disc and environment, respectively); boundary conditions are as follows:

$$\frac{\partial T}{\partial r} = 0 \quad \text{at } r = 0; \tag{3}$$

$$\lambda \frac{\partial T}{\partial r} + \alpha T = 0 \quad \text{at } r = r_2. \tag{4}$$

Analysis of calculations, given in [1], shows that electromagnetic shielding of the specific power of heat sources at disc edge significantly influences the uniformity of its distribution along the radius, particularly over the width of the hardfacing zone ($r_2 - r_3 = 10$–50 mm). If thermal shielding is also implemented at disc edge (see Figure 1), the heat flow through the edge will be significantly reduced or stopped completely, which will strongly influence the level of temperature distribution in the hardfacing zone, and the heat losses through the edge will also be reduced.

In the case of electromagnetic shielding of disc edge formula (1) may be expressed as follows:

$$w = \frac{\sigma\omega^2\mu_0^2}{128\pi^2 h} \times \left[\Delta I_1^2 A^2 a_1^2 + \Delta I_2^2 a_2^2 B^2 + K_{sh} 4ha_1^2 I_1^2 C^2 e^{(-2(r_2 - r))/\Delta}\right], \tag{5}$$

where K_{sh}, the coefficient of electromagnetic shielding for a shield, located close to the disc [5], has the following form:

$$K_{sh} = \exp\left(-2\frac{d_{sh}}{\Delta_{sh}}\right), \tag{6}$$

where d_{sh} is the shield thickness; $\Delta_{sh} = \sqrt{2/(\omega\mu_{sh}\sigma_{sh})}$ is the depth of electromagnetic field penetration into the shield; σ_{sh} is the electric conductivity of the shield material.

Assuming shield thickness $d_{sh} = \Delta_{sh}$, the power of heat sources on disc edge will decrease e^2 times, if $d_{sh} = 2\Delta_{sh}$, it will decrease e^4 times, at $d_{sh} = 4\Delta_{sh}$ it will decrease e^8 times (i.e. it will be practically zero). At $K_{sh} = 0$ we achieve full electromagnetic shielding, at $K_{sh} = 1$ the shielding is absent.

When a thermal shield is also installed at disc edge, boundary condition (4) has the following form:

$$\lambda \frac{dT}{dr} + K_t \alpha T = 0 \quad \text{at } r = r_2, \tag{7}$$

where K_t is the coefficient of thermal shielding [6], which varies in the range of $0 \le K_t \le 1$. At $K_t = 0$ we have full thermal shielding, at $K_t = 1$ the shielding is absent. Coefficient of thermal shielding, when using a shield of thickness d_t, will be found from the following relationship [6]:

$$K_t\alpha = \frac{\lambda}{d_t}; \quad K_t = \frac{\lambda}{d_t\alpha}, \tag{8}$$

where λ/d_t is the coefficient of heat conductivity of the shield.

If $\lambda/d_t = \alpha$, then $K_t = 1$, i.e. shielding is absent, an intensive convective heat exchange with the environment is in place and boundary condition (7) has the form of equation (4).

Let us assume that at the initial moment of time the disc temperature is equal to that of the environment. Then, initial condition for equation (2) will be expressed in the following form:

$$T = 0 \quad \text{at} \quad t = 0. \tag{9}$$

Solution of equation (2) at boundary condition (7) and initial condition (9) in the case, when the specific power is determined from formula (5), has the following form:

$$T = \frac{a}{\lambda_g}\sum_{\nu=1}^{\infty}\left(e^{-a\lambda_\nu^2 t}\int_0^t \frac{\int_0^{r_2} w(r, t)J_0(l_\nu, r)rdr}{\int_0^{r_2} J_0^2(l_\nu, r)rdr} e^{a\lambda_\nu^2 t_{dt}}\right) J_0(l_\nu, r), \tag{10}$$

where $l_\nu^2 = \lambda_\nu^2 - m^2$; $\lambda_\nu = \sqrt{l_\nu^2 + m^2}$; $J_0(l_\nu, r)$ is the Bessel function of the first kind of zeroth order of the real argument; a is the thermal diffusivity; l_ν are the roots of the characteristic equation

$$\lambda l_\nu J_1(l_\nu, r_2) + \alpha K_t J_0(l_\nu, r_2) = 0. \tag{11}$$

Thus, a mathematical model is obtained of determination of temperature in the disc through the source of its induction heating, using electromagnetic and thermal shielding of disc edge. This allows determination and optimizing the above temperature in the zone of disc hardfacing, depending on the parameters of the inductor, disc, electromagnetic and thermal shields, as well as electric current.

To optimize the parameters of the inductor and electric current, flowing through it, it is necessary to optimize the following functional:

$$\Phi = \int_0^{\tau}\int_{r_3}^{r_2} (T - T_{h.d})^2\, rdrdt, \tag{12}$$

where $T_{h.d}$ is the temperature at which sound hardfacing of a powder-like hard alloy on the working surface of the disc is performed; T is the temperature, which is determined from formula (10).

As the expression for specific power $w(r, t)$ includes all the design parameters of the inductor (h_1, h_2, $2h$, a_1, a_2, r_2) and electric current flowing through it, as well as of the electromagnetic field, induced by it, then, implementing the process of functional minimizing (12) by the required parameters, we obtain the optimum variant of the design of the inductor and electric current source to provide the technological process of induction heating simultaneously over the

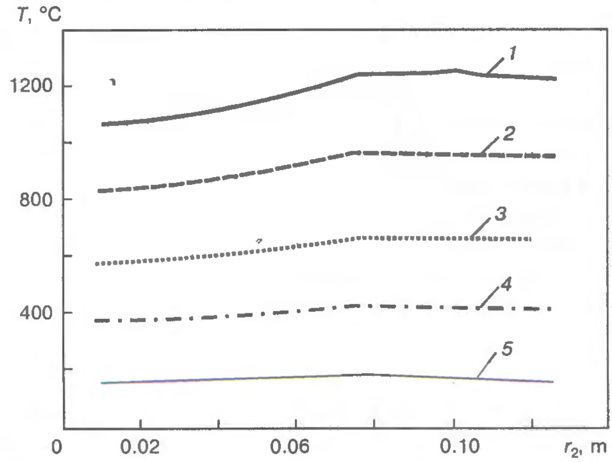

Figure 3. Temperature distributions around disc radius: r_2 = = 0.125 m for different moments in time: *1* — 22; *2* — 19; *3* — 15; *4* — 11; *5* — 5 s

Results of temperature calculation (°C) in different moments of time, depending on disc radius

r_2, m	τ				
	5	11	15	19	22
0.010	129.82	347.82	543.63	792.95	1023.71
0.020	131.79	352.20	550.40	802.74	1036.20
0.030	133.33	357.25	558.69	815.69	1052.42
0.040	137.38	367.11	573.66	836.58	1079.77
0.050	140.55	376.76	589.08	859.19	1108.96
0.060	145.98	390.55	610.06	889.09	1146.96
0.070	150.74	402.31	627.75	914.10	1178.64
0.075	155.25	412.48	624.39	934.13	1199.76
0.080	154.59	410.35	639.98	931.55	1202.21
0.090	154.01	411.21	641.67	934.36	1204.68
0.095	152.86	411.99	641.96	935.54	1205.64
0.100	154.90	413.08	644.25	937.72	1205.64
0.105	154.57	412.16	642.79	935.57	1205.93
0.110	154.62	411.99	641.96	934.56	1201.72
0.120	156.55	413.50	642.76	933.56	1201.99
0.124	157.89	414.78	643.65	933.87	1201.74
0.125	157.67	414.10	642.54	932.22	1199.59

entire working surface of a thin round and shaped disc.

As an example of calculation of the inductor, allowing for the design features and optimization capabilities, let us assign the geometrical dimensions of the heating system: radius of the inductor external turn $a_1 = 0.131$ m (see Figures 1 and 2), criterion $B_i = 0.27$ for a thermal insulation material on the external contour of the disc of asbestos sheeting of thickness $d_t = 0.004$ m, radius $r_3 = 0.075$ m (see Figure 1), hardfacing time $\tau = 22$ s, $\lambda = 0.35$ W/(m·°C).

Experimental data confirms that hardfacing temperature $T_1 = 1220$ °C. Then, at $T_{en} = 20$ °C we have $T_{h.d} = 1200$ °C. If the electromagnetic shield is made of copper, at circular frequency $\omega = 2\pi\cdot 440$ kHz the depth of the electromagnetic field penetration into the shield is $\Delta_e = 0.1$ mm.

Let us assume a_2, h_2, h_1, A, K_e to be the optimization parameters. Performing the procedure of functional minimizing by these parameters, we obtain their values: $a_2 = 0.0945$ m; $A = 165.20$; $K_e = 0.655$; $h_2 = 0.0315$ m; $a_1 = 0.131$ m; $h_1 = 0.01$ m; $r_3 = 0.075$ m.

Results of temperature calculations in the disc area at these values in different moments of time are given in the Table, and their graphic representation — in Figure 3. It can be seen from the Figure that the temperature is almost the same across the width of the hardfacing zone (in this case $S = r_2 - r_3 = 0.125 - 0.075 = 0.05$ m), deviation from the specified temperature being 0.5 %, and it is equal to 1200 °C over time $\tau = 22$ s (which is highly important at induction hardfacing). As the hard alloy (for instance, PG-S1) melts from the surface of the base metal, the thickness of the deposited metal is uniform over the entire working surface.

It follows from the conducted analysis that the final (at $\tau = 22$ s) temperature in the hardfacing zone in this case deviates from the required one by not more than 0.5%. For implementation of the found optimum coefficient of electromagnetic shielding $K_e = 0.655$ it is sufficient, according to formula (6), to use a copper plate of thickness $d_e = 0.021$ mm, i.e. spraying of copper powder onto the thermal shield or pasting of copper foil of the same thickness on it can be performed in practice.

The following data are assumed in calculations:

- for disc: $2h = 3$ mm; $c = 846$ J/(kg·°C); $\lambda = 40$ W/(m·°C); $\gamma = 5969.2$ kg/m^3; $\sigma = 1.25\cdot 10^{-6}$ 1/(Ohm·m); $r_2 = 0.125$ m; $\alpha = 455$ W/(m^2·°C); $r_3 = 0.075$ m; $\tau = 22$ s; $T_{h.d} = 1200$ °C. Base metal is steel St3, deposited layer is of alloy PG-S1, thickness of deposited metal is 0.8–1.5 mm;
- for inductor (copper): $\mu = 2.75\mu_0$; $\varepsilon_0 = 8.854\cdot 10^{-12}$ F/m; $\mu_0 = 4\pi\cdot 10^{-7}$ H/m; $\omega = 2.763\cdot 10^{-6}$ Hz; $c_1 = 5.0$ mm; $c_2 = 8.0$ mm; $\rho = 0.17\cdot 10^{-7}$ Ohm·m;
- for electromagnetic shield (copper):

$$\sigma_e = \frac{1}{\rho} = \frac{1}{0.17\cdot 10^{-7}} = 58.8\cdot 10^6 \text{ 1/(Ohm·m)};\quad \mu_e = \mu\mu_0 = 1\cdot 4\pi\cdot 10^{-7} = 12.56\cdot 10^{-7} \text{ H/m};\ K_e = 0.655.$$

For thermal shield (asbestos sheeting): $d_t = 0.004$ m; $\lambda = 0.35$ W/(m·°C); $\alpha = 455$ W/(m^2·°C); $K_t = \lambda/(d_t\alpha) = 0.192$.

CONCLUSIONS

1. The derived mathematical model for determination of the temperature in the disc through the parameters of a two-turn ring inductor, which is used to perform heating with electromagnetic and thermal shielding, allows optimizing the above temperature in the zone of disc hardfacing, depending on the parameters of the inductor, disc, electromagnetic and thermal shields, as well as electric current in the inductor.

2. Developed algorithm also allows designing the heating system (inductor, thermal and electromagnetic shields, part), which provides the required conditions for performance of the technological process of hardfacing.

3. The developed heating system ensures the required temperature in the hardfacing zone with the accuracy of up to 0.5 %.

4. A procedure has been developed for finding the coefficients of the electromagnetic and thermal shields, which are used for temperature regulation across the width of the hardfacing zone with a complex geometrical shape of the surface.

1. Shably, O.M., Pulka, Ch.V., Pismenny, A.S. (2002) Optimisation of inductor parameters for uniform heating of discs across the width of the hardfacing zone, allowing for screening. *The Paton Welding J.*, **11**, 23–25.
2. Shably, O.N., Pulka, Ch.V., Mikhajlishin, M.S. et al. *Device for power control in zone of hardfacing*. Positive decision on issuing of patent on application 2002119491. Filed 28.11.02.
3. Shably, O.N., Pulka, Ch.V., Pismenny, A.S. (1997) Optimisation of design parameters of inductor for induction hardfacing of thin steel discs. *Avtomatich. Svarka*, **6**, 17–20.
4. Shably, O.N., Pulka, Ch.V., Budzan, B.P. (1987) Optimisation of power consumption during induction hardfacing of thin-walled discs. *Ibid.*, **1**, 36–39.
5. Semyonov, N.A. (1973) *Technical electrodynamics*. Moscow: Svyaz.
6. Isachenko, V.P., Osipova, V.A., Sukomel, A.S. (1981) *Heat transfer*. 4th ed. Moscow: Energoizdat.

EFFECT OF ELECTRODE MATERIAL ON A SIGN OF TOTAL NEAR-ELECTRODE DROP OF VOLTAGE

D.M. KALEKO
E.O. Paton Electric Welding Institute, NASU, Kyiv, Ukraine

It is shown that the sign and value of difference of potentials between closing electrodes (sum of near-electrode drops of voltage) depend mainly on thermophysical properties of the cathode material.

Keywords: *electric arc, total near-electrode drop of voltage, cathode material*

In closing of low-current arc electrodes the interelectrode difference of potentials can either undergo a jump or reduce smoothly to zero [1]. In the first case the difference of potentials can change a sign. At the same time at opening of electrodes (mechanical jump at shock closing) the potential between them is always changed jumpy, increasing from zero to a positive value corresponding to usual voltage between electrodes before the arc column formation. It was revealed that a final value in a jumpy decrease of difference of potentials depends on the material of electrodes. Analysis of experimental data showed that sign and value of difference of potentials at the moment, preceding the contact of electrodes, are correlated only with the boiling temperature of the cathode material, i.e. easily-evaporating component of alloy (Figure 1). The similar correlation was observed in analysis of voltages of burning high-current vacuum arcs on pure metals (Figure 1, *b*) [2]. Aluminium and titanium are the only exception in a general regularity, as they provide stable compounds with oxygen, reducing the conductivity [3] and increasing the arc voltage [4].

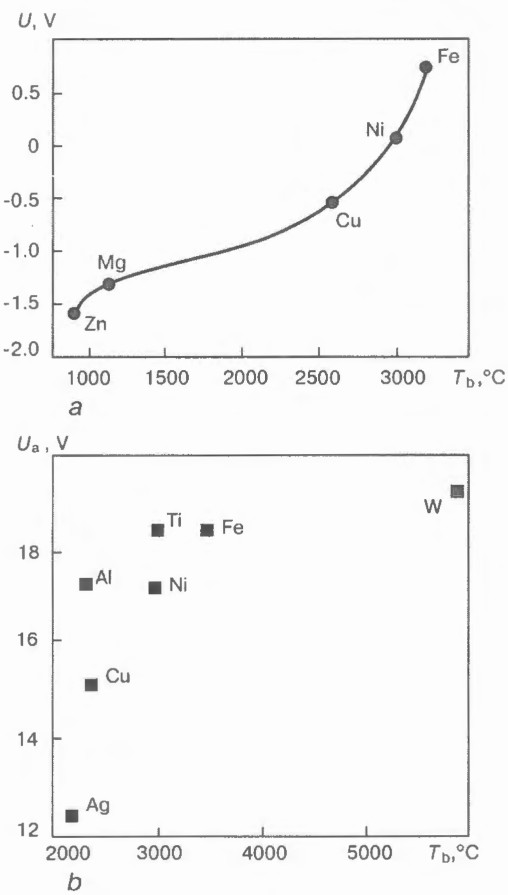

Figure 1. Dependence of voltage between contacting electrodes on boiling temperature of cathode material (low-temperature element of alloy) (*a*) and arc voltage on boiling temperature of metal of electrodes (*b*)

It is shown by calculations in assumption of dominating of a chaotic distribution of electron current near anode [5, 6] that at currents of more than 50 A a negative anodic barrier is realized in an anode layer of a space charge. A conclusion is made that anode potential is lower in most cases than potential of space charge in anodic region in high-current arc discharges at pressure values close to atmospheric values.

In the above-mentioned works the electric discharges were not considered in vapours of metal of electrodes, increasing the heat conductivity of the medium. As in these conditions the preheating of electrons by the field is required to maintain the current, then the anode drop of voltage should be positive [7]. In [8], at assumption of absence of ion current from arc column to anode, a good coincidence of calculated coefficients of melting anodes from different materials in the conditions of welding heating with experimental data was shown. Moreover, it was assumed that electrode material does not influence the level of anode drop of voltage, equal to 2.5 V.

Arc structure is accepted to be presented schematically as is shown in Figure 2, *a* [9–11]. Here, the space charges are considered either as independent formations, or as regions of arc column, faced the appropriate electrodes. In electrodes closing the arc column is, first of all, constricted, thus leading to decrease in voltage between the electrodes. Finally, the moment is started when the arc column is degenerated into two space charges (Figure 2, *b*).

The further change in voltage is associated with the recombination of space charges. Taking into account that the negative space charge is created because of a polarization of arc column under the effect of the anode potential, and the positive space charge is also

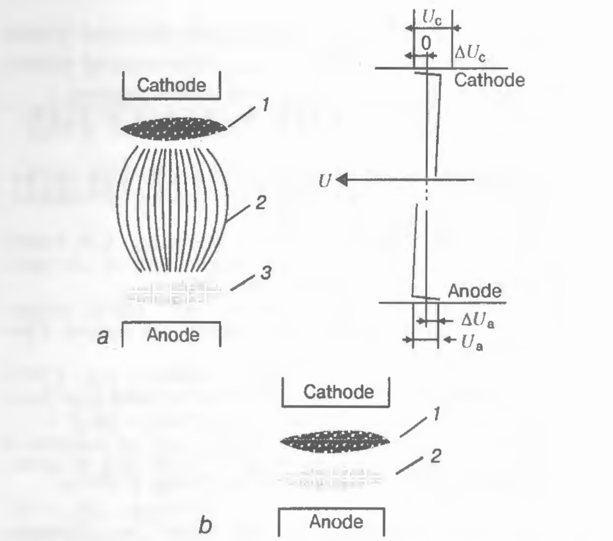

Figure 2. Schematic diagram of representation of arc discharge (*a*) and scheme of condition of interelectrode gas before its closing (*b*): *1* — space positive charge; *2* — arc column; *3* — space negative charge; U_c and U_a — cathode and anode potentials, respectively; ΔU_c and ΔU_a — potentials of space charges, respectively, in cathode and anode regions

affected by a comparatively low rate of ions, it is possible to assume that the charge near cathode has a higher absolute value than that near anode. This is confirmed by a high cathode drop of voltage as compared with an anode near-electrode potential [12–14].

The directed rate of ions depends on the displacement resistance. The higher density of vapours near cathode, the lower rate of diffusion of ions to cathode and larger space positive charge.

Taking into account that all the emitted electrons realize ionization [15], and the process of recombination occurring in a length of electron path is much higher than the process of ionization (typical sections of ionization are $1\cdot10^{-16}$ cm^2, recombinations — $1\cdot10^{-21}$ cm^2 [15]), the function of ionization can be presented in the form

$$F_i = n\,\sigma_i\,j_e = n_i\left(1 - D_i\,\frac{dn_i}{dx}\right), \tag{1}$$

where n is the density of neutral atoms in near-cathode region; n_i is the density of ions; σ_i is the section of ionizing; j_e is the density of electron current from cathode per time unity; D_i is the coefficient of diffusion of ions, which is equal in approximation of Chaplin-Ensky [16] to

$$D_i = \frac{3\sqrt{kT}}{8n\sqrt{\pi M}\sigma_r}. \tag{2}$$

Here, M is the ion mass; σ_r is the section of resonance recharging of ion on atom ($\sigma_r = 5\cdot10^{-19}$ m^2) [16]; T is the particle temperature.

Potential of the space charge is

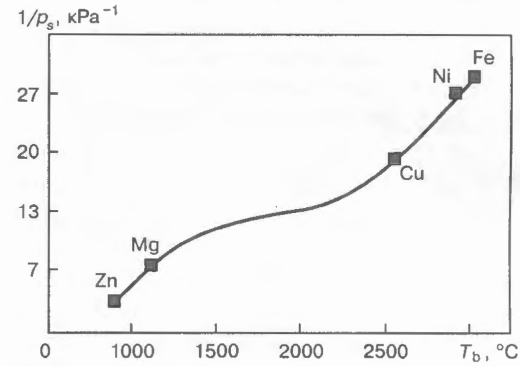

Figure 3. Inverse value of pressure of saturated gas of investigated metals

$$\varphi = 4\pi n_i e, \tag{3}$$

where e is the ion charge (probability of a multiple ionization is neglected due to its insignificance and calculations of estimating nature).

Density of neutral atoms near the evaporating cathode can be determined from the following equation:

$$n = \frac{p_s}{kT}, \tag{4}$$

where p_s is the pressure of a saturated vapour which can be calculated by formula

$$\log p_s = -\frac{A}{T} + B + C\log T;$$

the constant values A, B and C are given in [17]. Result of the mentioned calculation is given in Figure 3.

Density of neutral atoms n and coefficient D_i, as the calculation shows, are changed, respectively, from $51\cdot10^{19}$ and $0.01\cdot10^{-12}$ m^2/s for zinc and to $1.463\cdot10^{19}$ and $0.79\cdot10^{-12}$ m^2/s for iron. Thus, it follows from comparison of Figures 1 and 3*, and also analysis of equalities (1)–(4) that with decrease in boiling temperature of the cathode material the positive space charge in the cathode region should increase. In addition, the decrease in boiling temperature leads to the reduction in mobility of ions and increase in the positive space charge.

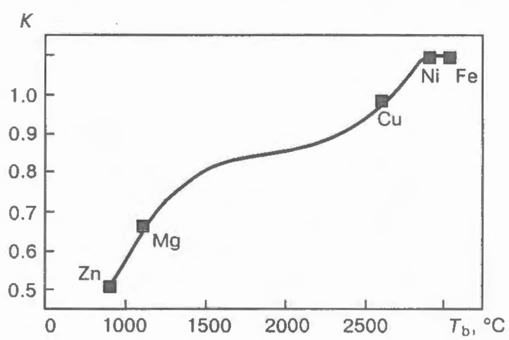

Figure 4. Dependence of K in equation (5) on T_b

* Some approach of points, corresponding to inverse values of elasticity of vapours of nickel and iron in Figure 3, as compared with Figure 1, is connected with the fact that the latter gives data for stainless steel, in which the partial pressure of chromium vapours increases the elasticity of vapours of the electrode metal.

Due to high pressure of vapours in the near-cathode region and large amount of collisions, the rates of gas particles are distributed by Maxwell and a kinetic theory can be applied to them, in accordance with which the amount of particles is determined by equation (4); mean square rate of particles $v = \sqrt{3kT/m}$; length of a free path of particle $\lambda = 1/\sqrt{2}\pi nS$.

Here, k is the Boltzmann constant; T is the temperature of a particle, taken with a good approximation equal to boiling temperature of the cathode material; m is the mass of particle; S is the section of collision, usually taken equal to a^2; a is the atomic «diameter».

As the values of mass and temperature of atoms of vapour and ions are almost equal, we can apply the above-given equations of the kinetic theory of gases to ions. Then, the ion mobility in electric field $b = \alpha e\lambda/mv$ can be presented in the form

$$b = \frac{\beta}{pa^2}\sqrt{\frac{T}{m}} = \frac{\beta}{p}K, \qquad (5)$$

where α and β are the numerical coefficients; $K = 1/a^2\sqrt{T/m}$.

Figure 4 shows values K for the investigated metals, which were calculated on the basis of data given in [17, 18].

Thus, the relationship, presented in Figure 1, finds an explanation in interaction of near-electrode space charges before closing the arc electrodes. Boiling temperature of the cathode material has the determinant effect on the positive charge. As the negative space charge is lower by an absolute value than the positive charge, the sign and value of potential between the closing electrodes (sum of near-electrode drops of voltage) depend on thermophysical properties of the cathode material.

Consequently, when determining the total near-electrode drop of voltage by changing the voltage between the approaching electrodes from the evaporating material [10], the values are obtained which are lower than real values by the difference of potentials of space charges in near-electrode regions.

1. Kaleko, D.M. (1995) On possibility to control the arc excitation in capacitor discharge stud welding. *Avtomatich. Svarka*, **7**, 21–24.
2. Borisov, V.N., Goncharov, V.K., Turomsha, E.P. (1988) Voltage of burning high-current vacuum arcs on pure metals. *Zhurnal Tekhn. Fiziki*, **8**, 1560–1562.
3. Bron, O.B., Lersky, B.A., Kuklev, Yu.V. (1978) Interaction of moving electric arc with ambient gas medium. *Elektrotekhnika*, **2**, 10–13.
4. Bukarev, V.A., Ishchenko, Yu.S., Erokhin, A.A. (1975) Some characteristics of arc in welding of 18-8 type steels with oxidised surface. *Svarochn. Proizvodstvo*, **10**, 3–4.
5. Merinov, N.S., Petrosov, V.A. (1976) Field of existence of arc burning condition with negative anode drop of potential. *Prikladn. Matematika i Tekhn. Fizika*, **1**, 17–24.
6. Dyuzhev, G.A., Nemchinsky, V.A., Shkolnik, S.M. et al. (1983) Anode processes in high-current arc discharge. *Khimiya Plazmy*, **10**, 169–209.
7. Bykhovsky, D.G., Korobova, I.L., Nemchinsky, V.A. et al. (1975) Thermal conditions of anode in AC welding arc of reversed polarity. *Avtomatich. Svarka*, **7**, 9–12.
8. Rabkin, D.M. (1951) Energy investigation of near-electrode zones of power welding arc. *Ibid.*, **2**, 3–5.
9. Granovsky, V.L. (1971) *Electric current in gas. Steady-state current*. Moscow: Nauka.
10. Leskov, G.I. (1970) *Electric welding arc*. Moscow: Mashinostroenie.
11. Samerwill, J.M. (1962) *Electric arc*. Moscow-Leningrad: Gosenergoizdat.
12. Matskevich, M.K., Bakuto, I.A., Bushik, A.I. et al. (1975) Determination of near-electrode drops of potential in high-current constricted arc. *Zhurnal Prikladn. Spektroskopii*, **6**, 1105–1107.
13. Sidorov, V.P. (1990) Procedure of evaluation of near-electrode voltages of «tungsten-aluminium» argon arc. In: *Abstr. of pap. of 4th All-Union Conf. on Welding of Non-Ferrous Metals*, Mariupol, Sep. 4–7, 1990. Kyiv: PWI.
14. Finkelnburg, V., Mekker, G. (1961) *Electric arcs and thermal plasma*. Moscow: Inostr. Literatura.
15. Bejlis, I.I., Lyubimov, G.A., Rakhovsky, V.I. (1969) Electric field at surface of electrode in cathode spot of arc discharge. *Doklady AN SSSR*, **3**, 552–555.
16. Eletsky, A.V., Palkina, B.M., Smirnov, B.M. (1975) *Phenomena of transport in weakly ionised plasma*. Moscow: Atomizdat.
17. Smitles, C.J. (1980) *Metals*. Refer. Book. Moscow: Metallurgiya.
18. Vol, A.E. (1959) *Structure and properties and binary metallic systems*. Moscow: Fizmatgiz.

INVESTIGATION OF THE PHASE FORMATION PROCESS IN DETONATION SPRAYING OF COMPOSITE POWDERS OF THE FeTi–B_4C SYSTEM

E.A. ASTAKHOV
E.O. Paton Electric Welding Institute, NASU, Kyiv, Ukraine

The paper gives investigation results on dependence of structure and phase composition of coatings produced by detonation spraying of the FeTi–B_4C system powders upon the powder preparation method. Significant differences were detected in morphology and composition of coatings produced by spraying of conglomerated and sintered powders. It is shown that the process of new phase formation proceeds more intensively in spraying of the conglomerated powders.

Keywords: *detonation spraying, phase composition, structure, conglomerated powder, sintered powder*

One of the areas of thermal spraying of coatings with increased wear and corrosion resistance is deposition of coatings consisting of a metal matrix reinforced with inclusions of particles of hard refractory compounds, such as carbides, borides and nitrides. For this, the above particles should be finely dispersed and uniformly distributed in the matrix [1–3].

Of interest from this standpoint is a combination of the spraying process with synthesis of a spray material accompanied by the exothermic effect. The presence of an internal heat source in formation of coatings should increase thermal activity of spray particles, ensure formation of a finely dispersed component of new phases and raise strength of adhesion of the coatings to the substrate.

Studies [1–3] consider different compositions in which interaction of components may occur under the self-propagating high-temperature synthesis conditions. It was established that the reaction of interaction of transition metals of groups IV–VI (e.g. titanium, zirconium, chromium etc.) with refractory nonmetallic compounds containing silicon, boron, carbon and nitrogen (e.g. SiC, B_4C, Si_3N_4 etc.) is accompanied by the exothermic effect that provides increase in temperature of a powder of the above system by 1500–2000 °C and more. The interaction products are silicides, borides, nitrides and carbides of metals, as well as complex ternary phases. Composite structures consisting, for example, of a silicide matrix with carbide or nitride inclusions may also be formed. The investigation results indicate to a promising future of this variant of the thermal spraying technology for deposition of coatings with an increased corrosion, heat and wear resistance.

This study is dedicated to the investigation of coatings produced by detonation spraying of composite powders of the FeTi–B_4C system. The choice of this system is based on the following consideration. Titanium carbide and boride are the compounds the formation of which under the self-propagating high-temperature synthesis conditions is accompanied by a high exothermic effect and adiabatic increase in temperature both in direct synthesis of elements [4, 5] and as a result of reaction of titanium with boron carbide [1, 2]. In formation of TiB_2, the process of interaction of titanium with B_4C causes an adiabatic increase in temperature amounting to 2869 °C.

Results of the experiments conducted to study the above effect by the differential thermal analysis method [6] show that the maximum exothermic effect is achieved in the case of using a mixture of 85FeTi + $15B_4C$ to form the interaction products of TiB_2, TiC, Fe_2B, Fe_3B and Fe_3C, which can act as the reinforcing phases in ferrotitanium. This composition of the mixture was chosen for preparation of the spray powders.

Two types of powders were utilised for spraying: conglomerated powder of raw materials with a binder [3] and powder sintered at 800 °C for 30 min in hydrogen and subjected subsequently to crushing to produce particles of a required size. According to the differential thermal curves of heating, no chemical interaction occurs during exothermic reactions in the FeTi–B_4C system at the above sintering temperature and time [3]. In this case the diffusion processes lead only to sticking of the B_4C particles to the surface of the FeTi particles. Polyvinyl alcohol (4 vol.% with respect to the charge mass) was used as a binder for conglomeration. Powders of ferrotitanium (44.8 wt.% Ti) and boron carbide with particles 40–100 and 5–40 μm in size (content of particles about 5 μm in size was approximately 70 vol.%) were used as raw materials.

Appearance and microstructure of the spray powders are shown in the Figure, *a–e*. Composite particles of FeTi–B_4C (*3*) and isolated particles of FeTi (*1*) and boron carbide (*2*) (Figure, *a–c*) are seen in structure of the conglomerated powder. Particles of the sintered powder are characterised by a higher cohesion strength compared with the conglomerated powder. However, they are porous and have cracks, which makes it impossible to measure their microhardness.

Spraying of the produced composite powders was performed using the automatic detonation unit «Perun-S». The gas mixture consisted of oxygen and pro-

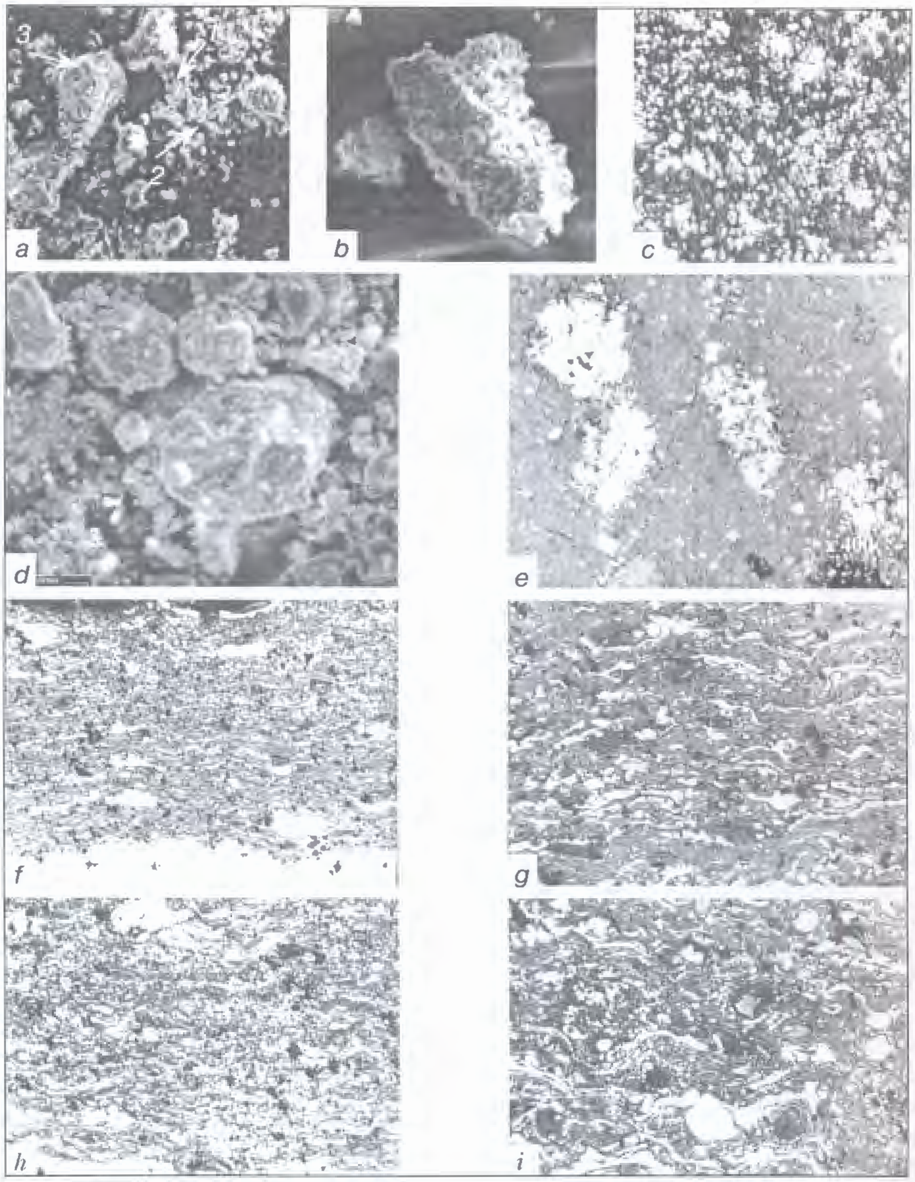

Appearance (*a*, *b*, *d*) and microstructure (*c*, *e*) of composite powders of the $FeTi-B_4C$ system, as well as microstructure of detonation coatings from the above powders (*f*–*i*): *a* (×400), *b* (×1000), *c* (×100), *f* (×250), *g* (×625) – conglomerated powder; *d*, *e* (×400), *h* (×250), *i* (×625) – sintered powder

pane-butane. Flow rate of the working gases is given in Table 1.

Microstructure of the coatings was examined using the metallographic microscope «Neophot-32» under different magnifications, and microhardness was measured using the LECO instrument M-400.

X-ray diffraction phase analysis of the coatings and powder entrapped while it was ejected from the unit channel was performed using the X-ray diffractometer «Dron-3» in the $K_\alpha Co$ radiation. This allowed tracing of the process of phase formation at a stage of interaction of powder with the detonation products (inside the unit channel) and during formation of a coating layer on the substrate. Microstructures of the deposited coatings are shown in the Figure, *f*–*i*.

Table 1. Conditions of the process of spraying of the FeTi–15 % B_4C system powders

Gas flow rate, m³/h	*Conglomerated powder*	*Sintered powder*
Propane-butane	0.50	0.55
Oxygen	1.30	1.30
Air	0.55	0.65

Coating from the conglomerated powder (Figure, *f*, *g*) is characterised by a high density and good adhesion to the substrate. The basic component of its structure is grey in colour with local regions of a yellow-brown shade. It is a set of different oxide phases (Table 2). Microhardness of this component varies from 5300 to 7700 MPa, which is in good agreement with the data of [7] for titanium and iron oxides. Isolated inclusions of the non-reacted B_4C particles characterised by a smooth and bright surface are also seen. A light metallic component of microstructure (not more than 15 %) has microhardness of 3000–5150 MPa and corresponds to FeTi and Fe_2Ti. It is of the three types: finely dispersed inclusions in the main grey phase, lamellae and isolated coarse, almost equiaxed inclusions. Structures of coatings from the sintered and conglomerated powders hardly have any qualitative difference. However, they have a bit different quantitative proportions of phase components. A grey phase seen in structure of the coatings (about 60 vol.%) is dense, containing fine embedments of particles of a white phase (Figure, *h, i*). Size of light-grey inclusions having a clearly defined boundaries and smooth surface is 4×4, 4×8 and rarely 4×16 μm. They are characterised by high microhardness (H_μ 20,000 MPa). Phase Fe_2Ti is present in the form of both lamellae 2–4 μm thick (sometimes 1–10 μm) and isolated particles from ≤ 1 to 45 μm in size. Grayish-brown inclusions of the oxide type and pink inclusions of the boride type are found inside the light particles.

Results of X-ray diffraction phase analysis (see Table 2) of the initial powders, powders entrapped after ejection from the unit channel and coatings allowed the following assumptions to be made concerning phase formation during spraying of the coatings. Titanium diboride TiB_2 was detected in a composition of the entrapped conglomerated powder. This fact indicates to occurrence of the reaction as early as inside the unit channel. In addition to TiB_2, also Ti_3B boride was detected in the coating. This is indicative of the fact that phase formation took place also at the moment of formation of a layer. In addition to borides, the entrapped conglomerated powders and the coating layer composed of them also contain titanium and iron oxides, as well as complex oxides of the Ti–Fe–O type. The presence of iron borides and carbides was not fixed, which is associated with a low exothermic effect of reactions of their formation.

In spraying of the sintered powder, only the oxide phases were detected in the entrapped powder, while the coating contained only one new boride phase TiB. Formation of other phases characterised by the highest thermodynamic stability (see Table 2) took place as early as during the process of sintering of the powder.

Table 2. Results of X-ray diffraction phase analysis of initial powders of the FeTi–15 % B_4C system and coatings produced from these powders

Test object	*Conglomerated powder*	*Sintered powder*
Initial powder	FeTi, B_4C, γ-Fe–Ti–O, Fe_2Ti, $B_{13}C_2$, TiO_2 (traces), TiC (traces)	Fe_2Ti, Fe_2B, TiB_2, Fe_2TiO_4, TiC, B_4C, β-TiO_2
Entrapped powder	FeTi, γ-Fe–Ti–O, $FeTiO_5$, TiB_2, B_4C, $B_{13}C_2$, TiO_2, Ti_2O_3 (traces), TiC (traces)	Fe_2Ti, $FeTiO_3$, TiB_2, TiO_2, Fe_2TiO_4, Fe_2B, TiC, B_4C
Coating	Fe_2Ti, FeTi, Ti_3B, TiB_2, Fe_2TiO_4, Fe_3O_4, TiO_2, Ti_3O_5, B_4C (traces)	Fe_2Ti, TiO, TiO_2, TiB_2, TiB

CONCLUSIONS

1. The results obtained prove that structure of the coatings produced by detonation spraying of composite powders of the FeTi–B_4C system comprise such synthesis products as borides TiB_2, Ti_3B and TiB.

2. Phase formation during detonation spraying was found to take place both during the process of interaction of the initial powder with the detonation products and during formation of the coating layer. Quantitative proportion of the formed phases depends upon the method of production of a composite powder.

3. In addition to the synthesis products, a coating contains also a number of oxide phases of titanium and iron, the formation of which is inevitable because of the presence of oxygen in a working detonation mixture.

4. High values of microhardness of the synthesis products and oxide phases, as well as their fine-dispersed distribution in the coating layer give ground to recommend composite powders of the FeTi–B_4C system for practical application during thermal spraying as a wear-resistant component of mechanical mixtures with nickel or iron alloys.

1. Borisova, A.L., Borisov, Yu.S., Shvedova, L.K. et al. (1980) Interaction between boron carbide and titanium under thermal and plasma heating conditions. *Poroshk. Metallurgiya*, **9**, 47–53.
2. Akoyan, A.G., Dolukhanyan, S.K., Borovinskaya, I.P. (1978) Interaction of titanium, boron and carbon under combustion conditions. *Fizika Goreniya i Vzryva*, **3**, 70–76.
3. Borisov, Yu.S. Borisova, A.L. (1986) *Plasma and powder coatings*. Kyiv: Tekhnika.
4. Maslov, V.M., Borovinskaya, I.P., Merzhanov, A.G. (1978) Experimental determination of maximum temperatures during the processes of self-propagating high-temperature synthesis. *Fizika Goreniya i Vzryva*, **5**, 79–85.
5. Kardashkin, A.I., Maksimov, Yu.M., Nekrasov, E.A. (1981) On the mechanism of interaction between titanium and carbon in a combustion wave. *Ibid.*, **4**, 33–36.
6. Grigorenko, G.M., Borisova, A.L., Borisov, Yu.S. et al. (2003) Investigation of interphase interaction of ferrotitanium with boron carbide in powder mixtures for deposition of thermal coatings. *Advances of Electrometallurgy*, **1**, 26–29.
7. (1978) *Physical-chemical properties of oxides*. Refer. Book. Ed. by G.V. Samsonov. Moscow: Metallurgiya.

ELECTRODES OF THE ANV SERIES FOR WELDING HIGH-ALLOY STEELS AND ALLOYS

K.A. YUSHCHENKO, Yu.N. KAKHOVSKY, G.V. FADEEVA, V.I. SAMOJLENKO and A.V. BULAT
E.O. Paton Electric Welding Institute, NASU, Kyiv, Ukraine

Described are the status and prospects of development and application of covered metal electrodes of the ANV grade intended for welding high-alloy steels and nickel-base alloys in chemical, power and transport engineering, food processing, chemical and metallurgical industries, cryogenic engineering and power generation.

Keywords: *arc welding, high-alloy steels, nickel-base alloys, covered metal electrodes, ANV grade*

Chemical production equipment operating under the effect of aggressive environments, high temperatures and pressures is manufactured by using three basic groups of high-alloy steels and alloys:

- corrosion-resistant Cr–Ni steels of the 12Kh18N10T type employed for the manufacture of vessel type facilities operating under conditions of oxidising environments, such as nitric, acetic, phosphoric and other acids, as well as alkali and salt solutions at a temperature of up to 600 °C. In the case of excessive pressure in the facilities the maximum permissible service temperature should be 350 °C [1, 2];
- Cr–Ni–Mo steels 10Kh17N13M2T (EI-448), 10Kh17N13M3T (EI-432) and 08Kh17N16M3T employed for the manufacture of vessel type facilities operating under the effect of non-oxidising environments, such as production of carbamide, caprolactam etc., at a temperature of about 170–190 °C and excessive pressure of up to 18 kPa. Steel 08Kh17N16M3T developed by the Irkutsk NIIkhimmash [2, 3] is most suitable for such production. Similar steels with a limited carbon content, i.e. 03Kh16N15M3 (EP-580), 03Kh17N14M3 (EP-844) and 03Kh21N21M4GB are applied for structures operating under the most severe conditions;
- Cr–Ni–Mo–Cu steels and alloys of the 06Kh23N28M3D3T (EI-943) type designed for the manufacture of vessel facilities used for production, transportation and storage of different concentrations of sulphuric acid, nitrophosca and wet-process phosphoric acid under conditions of service temperature of up to 80 °C, except for 55 % phosphoric and acetic acids [3, 4].

Electrodes of more than 30 grades differing in both chemical composition of deposited metal and covering type are used in the CIS countries for welding Cr–Ni steels. The drawback the majority of them share is a comparatively low level of welding-operational properties. Thus, electrodes of the basic type, i.e. OZL-8, TsL-11 and TsT-15, are characterised by a low stability of the arc burning process, increased spattering and globular transfer of electrode metal with short-circuiting of the arc gap. They are employed only for welding at a direct current. The improved stability of the arc burning process is provided by electrodes of the OZL-36 grade with a covering of the rutile-basic type. However, in this case formation of vertical and overhead welds is much worse than that provided by the TsL-11, TsT-15 and OZL-8 electrodes. Electrodes of the OZL-14A grade with a rutile type covering, allowing welding to be performed at both direct and alternating current, are characterised by more favourable welding-operational properties. Welding with the above electrodes can be performed only in the flat position using welding transformers (at increased open-circuit voltage $U_{o.-c} \approx 80$ V), which certainly leads to a limitation of their application field.

The E.O. Paton Electric Welding Institute has been active for many years in development of highly practicable electrodes, allowing welding to be performed at both direct and alternating current in all spatial positions, and providing an easy repeated ignition of the arc, good weld formation (fine-ripple surface structure with no convexity of the weld bead), easy slag crust detachability, minimal losses of electrode metal for spattering, and better sanitary-hygienic characteristics, compared with electrodes of the basic type.

These requirements are met by electrodes of the ANV-29 (E-07Kh20N9) grade with rutile-basic covering [5] intended for welding of parts from steels of the 12Kh18N10T type. These electrodes are used in the cases where no requirements for intercrystalline corrosion (ICC) resistance are imposed on welded joints (Table 1). The electrodes provide good weld formation in welding in all spatial positions at both direct and alternating current, easy slag detachability and minimal (to 1 %) spattering of the electrode metal.

In addition, electrodes ANV-29 provide a spray transfer of the electrode metal at a duration of short circuits of the arc gap equal to no more than 8 ms. In the case of welding with basic electrodes this value amounts to 20 ms. Decrease in size of droplets and reduction of the time during which they transfer to the weld pool lead to lower losses of thermal power for overheating of the electrode metal and higher elec-

Table 1. Characteristics of covered electrodes for welding corrosion-resistant steels and alloys

Welded steel grade	*CIS electrodes*	*ANV series electrodes*	*Welding current for ANV electrodes*	*Mechanical properties of metal*				*ICC resistance*
				σ_t, *MPa*	σ_y, *MPa*	δ_5, *%*	*KCU, J/cm²*	
12Kh18N10T	OZL-8	ANV-29	DC, AC	≥ 500	≥ 280	≥ 30	≥ 100	Not specified
	TsL-11	ANV-35		≥ 500	≥ 356	≥ 22	≥ 80	Ensured
08Kh17N13M2T	EA 400/10u	ANV-17	DC	≥ 550	≥ 250	≥ 30	≥ 120	Same
08Kh17N13M3T	NZh-13			≥ 600				
03Kh23N28M3D3T	OZL-17u	ANV-28	Same	≥ 550	≥ 280	≥ 26	≥ 70	»
06KhN28MDT		ANV-42						
02Kh8N20S6	OZL-24		»	≥ 588	≥ 461	≥ 20	≥ 60	»
08Kh22N6T	TsL-11	ANV-33MB	DC, AC	≥ 588	≥ 440	≥ 26	≥ 100	»
08Kh22N6M2T								

trode melting rate, the deposition efficiency amounting to 13–14 g/(A·h).

Rutile-basic electrodes ANV-35 (E-08Kh20N9G2B type) characterised by additional alloying of the weld metal with niobium [5], which are similar to electrodes ANV-29 in their welding-operational properties, were developed for welding of parts resistant to ICC. Electrodes ANV-29 and ANV-35 comply with the requirements of GOST 10052–75, GSTU 3-17-191–2000, GSTU 3-020–2001 and other standards in chemical composition of the deposited metal, mechanical properties of the weld metal and welded joints, as well as general corrosion and ICC resistance.

Worthy of notice among Cr–Ni steels are steels of the 03Kh18N11 type with a decreased carbon content, characterised by the highest corrosion resistance. Electrodes ANV-13 [6] and OZL-22 with rutile-basic and basic coverings are used for welding such steels. These electrodes can be employed for welding only at a direct current in all spatial positions, except for the overhead position.

Equipment from steels 10Kh17N13M2T, 10Kh17N13M3T and 08Kh17N16M3T is manufactured by using basic electrodes EA-400/10u (E-10Kh18N11G2F) and NZh-13 (E-09Kh19N10G2M2B), which are characterised by the same drawbacks as electrodes TsL-11, TsL-15 and OZL-8, i.e. low arc stability, increased spattering and globular transfer of electrode metal with short-circuiting of the arc gap. Welding using these electrodes can be performed only at a direct current. Electrodes NZh-13 used for welding of the above Cr–Ni–Mo steels provide high ICC resistance of the weld metal owing to its stabilisation with niobium. In this case the high technological strength of the weld metal is ensured by 2 to 10 % of the ferritic phase present in them. However, in a number of cases (carbamide and caprolactam production) this may have a negative effect on general corrosion resistance due to structurally selective corrosion of the ferritic component.

To avoid the above drawbacks, the E.O. Paton Electric Welding Institute developed for mechanised arc welding a fundamentally new system of alloying of the weld metal and, based on this system, offered wire of the Sv-01Kh19N18G10AM4 (EP-690) grade additionally alloyed with nitrogen and manganese. A low carbon content (to 0.03 %) and an optimal proportion of chromium, nickel and molybdenum provide a sufficient general corrosion resistance and ICC resistance in non-oxidising environments, while the additional alloying with manganese and nitrogen provides a high technological strength of the weld metal.

High-oxidising flux AN-18 was also developed for mechanised arc welding of Cr–Ni–Mo steels using wire EP-690. The use of this flux allowed an additional decrease in carbon and silicon content of the deposited metal.

The above successful technological solutions were used as the basis for the development of fundamentally new electrodes of the ANV-17 (E-02Kh19N18G5AM3) grade (Table 1). These electrodes have a rutile-basic covering containing up to 10 % of chromium oxide, which provides a low carbon and silicon content of the deposited metal. The decreased carbon content has a positive effect on general corrosion resistance of welded joints and ICC resistance, while a decreased silicon content leads to increase in technological strength of the weld metal, especially in welding of structures more than 20–22 mm thick.

Electrodes ANV-17 are extensively used now in chemical engineering at enterprises of Ukraine and other CIS countries. It should be noted that along with electrodes ANV-17, Cr–Ni–Mo steels with a decreased carbon content are welded using also basic electrodes OZL-20 and OZL-26A. These electrodes can be employed for welding only at a direct current, which limits the possibility of their application for repair operations.

The E.O. Paton Electric Welding Institute is active in research and development for upgrading electrodes ANV-17. Positive results have been obtained in DC welding with the new rutile-basic electrodes in all spatial positions. Pilot Plant for Welding Consumables of the Institute is mastering production of these electrodes.

Electrodes OZL-17u and OZL-37 based on wire Sv-01Kh23N28M3D3T (EP-516) with a covering of the CaF_2–TiO_2–$CaCO_3$ type are employed until now for welding Cr–Ni–Mo steels and alloys of the 06KhN28MDT (EI-943) grade. It should be noted that welding of alloy EI-943 with electrodes OZL-17u provides both general corrosion and ICC resistance. However, no success has been achieved so far in welding thick-plate structures with a required technological strength, as the welds in this case are susceptible to cracking in reheating.

To solve this problem, the E.O. Paton Electric Welding Institute developed covered electrodes and a welding method [7, 8] providing for making load-carrying layers of a welded joint (70–80 % of section) by using austenitic-ferritic metal of electrodes ANV-17 and facing layers (on the side of impact by an aggressive environment) – by using electrodes ANV-28 [9] or ANV-42. These electrodes have a basic covering and are intended for DC welding in all spatial positions.

The work is in progress on development of improved electrodes for welding and repair of actual parts from alloy EI-943.

In addition to the above materials, in chemical engineering the use is made also of Cr–Ni–Si steels and two-phase austenitic-ferritic steels sparsely alloyed with nickel.

Cr–Ni–Si steels (of the type of 02Kh8N20S6) are applied in metal structures intended for production and storage of concentrated (≈ 98 %) nitric acid at a temperature of up to 100 °C [10]. Welded joints in the above steels are susceptible to ICC in the HAZ and knife-line corrosion in the fusion zone. To eliminate fracture of this type, welded joints are subjected to heat treatment, i.e. austenisation from 1050 °C and water quenching. Often there is no way for performing this heat treatment under factory conditions. This is especially the case of fabrication of large-size process equipment.

The E.O. Paton Electric Welding Institute completed the package of work that allowed the above problems to be solved through improving steel 02Kh8N20S6 (by additionally alloying it with niobium), and through developing filler wire EK-76 for manual tungsten-electrode arc welding [11].

It should be noted that basic electrodes OZL-24 are also employed for manual arc welding of Cr–Ni–Si steels. These electrodes are intended for welding only at a direct current of reverse polarity.

Two-phase austenitic-ferritic steels sparsely alloyed with nickel (08Kh22N6T and 08Kh21N6M2T) are applied in structures of units used for production of weak nitric acid, pulp-and-paper industry equipment and heavy-loaded separators. These steels have a number of advantages over austenitic ones, such as higher strength, increased ICC and stress corrosion resistance [12]. The E.O. Paton Electric Welding Institute studied peculiarities of welding and properties of welded joints in the above steels. It was shown [1] that the austenitic-ferritic steels with 20–22 % Cr should contain 40–60 % of the ferritic phase to eliminate ICC and structurally selective corrosion, and ensure general corrosion resistance. At 0.07 % C, in the presence of niobium and titanium the content of nickel should be 6–7 %. Keeping to the above requirements provides desirable mechanical properties of welded joints and hot crack resistance of the welds.

Rutile-basic electrodes ANV-33MB were developed for welding the above steels. These electrodes can be used for welding at both direct and alternating current in all spatial positions. In this case also basic electrodes TsL-11 can be used, although they are intended for welding only at a direct current of reverse polarity.

High-manganese steels find wide application in mining, metallurgical, transport, construction and other industries owing to their unique physical-mechanical properties, including at low temperatures [13]. In metal structures, they are used as a rule in combination with other steels, e.g. low- and medium-carbon and low-alloy ones.

Welding of high-manganese steels of the 10Kh14G14N4T (EI-711), 45G17Yu3 and 110G13L types, as well as dissimilar (low-alloy) steels to Cr–Ni steels of the austenitic grade is performed using electrodes of the NII-48G grade. As a substitute for these electrodes, the E.O. Paton Electric Welding Institute developed electrodes ANV-27 which were extensively used in mining machine building of the former USSR [14]. New electrodes of the ANV-66 (E-10Kh20N9G6) grade characterised by improved welding-operational properties, such as easy repeated ignition of the arc, its stable burning and low metal losses for spattering, have been developed during the last years. They provide good weld formation at a deposition efficiency of 14–16 g/(A·h) (Table 2) and can be used for welding at both direct and alternating current in all spatial positions (open-circuit voltage of a welding transformer is less than 70 V). Electrodes ANV-66 have been applied at Makrokhim Ltd. in Mariupol and at Open Joint-Stock Company «Lenzoloto» in Yakutia.

Isothermal tanks of ferritic steels ON6 and ON9, which successfully compete with more expensive austenitic steels, are applied for storage and transportation of liquefied gases (natural gas, nitrogen and oxygen) at temperatures down to −196 °C [15]. Welding of metal structures of such tanks is performed by using mostly high-nickel filler metals, such as electrodes OZL-25B (E-10Kh20N70G2M2B2V) with a covering of the basic type. Welding using these electrodes is carried out at a direct current in all spatial positions. However, in a number of cases they fail to provide sufficient porosity resistance and induce problems associated with arc blow.

The E.O. Paton Electric Welding Institute developed more economical basic electrodes of the ANV-45

Table 2. Characteristics of covered electrodes for welding high-manganese, heat-resistant and cryogenic steels and alloys

Welded steel grade	*CIS electrodes*	*ANV series electrodes, Ukraine*	*Welding current for ANV electrodes*	*Mechanical properties of metal*				*ICC resistance*
				σ_t, *MPa*	σ_y, *MPa*	δ_5, *%*	*KCU, J/cm²*	
45G17Yu3, 10Kh14G14N4T, 110G13L and dissimilar joints	NII-48G	ANV-66	DC, AC	≥ 590	≥ 280	≥ 20	≥ 120	Not specified
03Kh20N16AG6	OZL-23B	ANV-45	Same	≥ 600	≥ 400	≥ 20	≥ 40	At *T* = 20 °C
ON6 and ON9							≥ 35	At *T* = –196 °C
20Kh23N13	OZL-6	ANV-70	»	≥ 590	≥ 340	≥ 25	≥ 120	Heat resistance up to 1000 °C
KhN78T	TsT-28	ANV-68	DC	≥ 600	≥ 280	≥ 20	≥ 100	Same

grade (E-08Kh19N18G8AM3), allowing welding in all spatial positions at both direct and alternating current, providing high porosity resistance and eliminating arc blow during the welding process (Table 2). Electrodes ANV-45 are recommended also for the manufacture of cryogenic equipment from austenitic steel 03Kh20N16AG6 [16].

The E.O. Paton Electric Welding Institute developed rutile-basic electrodes ANV-70 (E-10Kh25N13G2) based on wire 07Kh25N13 (Table 2) to be used as a substitute for electrodes OZL-6 for welding heat-resistant steels 20Kh23N13 (EI-319) and 20Kh23N18 (EI-417) operating under the effect of oxidising environments at temperatures of up to 1000 °C and dissimilar steels (low-alloy) to steels of the austenitic grade, as well as chrome steels of the 15Kh25T type (EI-439). They allow welding to be performed both at direct and alternating current in all spatial positions, provide easy repeated ignition of the arc, good weld formation, easy slag crust detachability, and are characterised by minimum losses of electrode metal for spattering.

Alloys of the KhN78T (EI-435) type are used to manufacture components of combustion chambers of gas turbines operating at temperatures of up to 1100 °C, and alloys KhN70VMYuT (EI-765) are used to manufacture components operating at temperatures of 750–800 °C [17]. Welding of these alloys is done by using basic electrodes TsT-28 (E-08Kh14N65M15V4G2) at a direct current in all spatial positions.

Basic electrodes ANV-68 (E-08Kh14N65M15V4G2) (Table 2) were developed as a substitute for electrodes TsT-28. The new electrodes allow welding to be performed at a direct current in all spatial positions, and they provide better slag crust detachability and lower losses of electrode metal for spattering.

Production of electrodes ANV-68 and ANV-70 is now mastered by the Pilot Plant for Welding Consumables of the E.O. Paton Electric Welding Institute of the NAS of Ukraine.

1. Kakhovsky, N.I. (1975) *Welding of high-alloy steels*. Kyiv: Tekhnika.
2. (1954) *Corrosion and chemical resistance of materials*. Refer. Book. Ed. by N.A. Dolezhal. Moscow: Mashgiz.
3. Tufanov, D.G. (1982) *Corrosion resistance of stainless steels and pure metals*. Refer. Book. 4th ed. Moscow: Metallurgiya.
4. Kakhovsky, N.I., Fartushny, V.G., Demianenko, G.P. (1968) Automatic submerged-arc welding of 0Kh23N28M3D3T steel. *Avtomatich. Svarka*, **8**, 47–51.
5. Yushchenko, K.A., Zakharov, L.S., Dyatlova, G.V. (1983) Versatile electrodes for high-alloy chrome-nickel steels of the 18-10 type. In: *Proc. of All-Union Conf. on Welding Consumables*, Cherepovets-Kyiv, 1983. Kyiv.
6. Kakhovsky, N.I., Lipodaev, V.N. (1965) Electrodes for welding of chrome-nickel stainless steels of the 18-10 type with low carbon content. *Avtomatich. Svarka*, **12**, 55–58.
7. Kakhovsky, N.I., Lipodaev, V.N. *Arc welding method*. USSR author's cert. 712210. Int. Cl. B 23 K 9/00. Publ. 05.03.80.
8. Kakhovsky, N.I., Lipodaev, V.N. *Arc welding method*. USSR author's cert. 791479. Int. Cl. B 23 K 9/00. Publ. 07.10.80.
9. Kakhovsky, N.I., Lipodaev, V.N., Ukolova, E.S. (1977) Electrodes for welding of stable-austenitic alloys EI-943 and EP-516. *Avtomatich. Svarka*, **7**, 68–69.
10. Agutina, N.A., Syguchyova, L.Kh., Lipodaev, V.N. et al. (1986) Corrosion resistance of welded joints from 02Kh8N22S6 steel in 98 % nitric acid. In: *New corrosion-resistant steels and alloys and corrosion protection*. Moscow: NIIkhimmash.
11. Lipodaev, V.N. Yushchenko, K.A., Skulsky, V.Yu. et al. (1985) Influence of nickel on structure and properties of high-silicon austenitic welds. *Avtomatich. Svarka*, **9**, 9–12.
12. Ulianin, E.A. (1981) Corrosion-resistant steels and alloys. In: *Coll. of pap. of Seminar on New Achievements in the Field of Theory and Practice of Corrosion Protection of Metals*, Zvenigorod, 1980. Moscow.
13. Bogachyov, I.N., Egolaev, V.F. (1973) *Structure and properties of iron-manganese alloys*. Moscow: Metallurgiya.
14. Lipodaev, V.N., Kakhovsky, N.I., Zakharov, L.S. et al. (1977) New sparsely-alloyed materials for welding steels 110G13L and 30G. *Avtomatich. Svarka*, **9**, 71–73.
15. Yushchenko, K.A., Starushchenko, T.M., Pestov, V.A. et al. (1986) Mechanised welding of cold-resistant steels with 6 and 9 % nickel. In: *Proc. of Int. Conf. on Cryogenic Materials and their Alloys*. Kyiv: Naukova Dumka.
16. Zakharov, L.S., Pestov, V.A., Samojlenko, V.I. (1990) Electrodes for AC welding of cold-resistant steels ON9 and ON6. In: *Proc. of 10th All-Union Conf. on Welding Consumables*, Krasnodar, 1990.
17. Zemzin, V.N. (1972) *Heat resistance of welded joints*. Leningrad: Mashinostroenie.

TECHNOLOGY OF BRAZING OF TUBULAR PACKS OF RADIATOR SECTIONS OF LOCOMOTIVES AT HOLDING COMPANY «LUGANSKTEPLOVOZ»

G.G. BASOV, A.N. TKACHENKO, A.A. SKORODUMOV and **N.P. EFIMOVA**
Holding Company «Luganskteplovoz», Lugansk, Ukraine

The design of a tubular pack of radiator sections is shown, the technology of its manufacture in a specialized equipment is described and prospects for improving the process of sintering are defined.

Keywords: *sintering, brazing, spreading of brazing alloy, wettability by brazing alloy, chamber, conveyor, automatic machine, flux, gas welding, test, capacity, fluxing*

The HC «Luganskteplovoz» is the leading enterprise for the production of sections of radiators of locomotives of all series and also of other machines and mechanisms. Sections of radiators are the main elements of the locomotive water system, providing the cooling of a diesel, blown air and oil. The industrial capacities of the enterprise are designed for the annual production of 160,000–170,000 sections of different modifications (heating, cooling, calorifers and also sections with turbulization). Technology of their manufacture is quite complicated and diverse, it is defined by design features of separate elements of sections (large number of connecting elements and small distance between them), and also combination of such materials as copper–brass–steel (different physical and chemical properties).

The most wide spreading model of a water-air radiator is a section of 1413 mm height, 153 mm width and 203 mm depth. Almost all the modifications of the radiator sections have a standard design, however, they are differed from each other by a pitch of plates arrangement, cross-section of tubes, dimensions and total mass. The basic element of a water radiator section (Figure 1) is a tubular pack (1220×151×91 mm), consisting of two semi-packs [1]. Semi-pack represents a set of copper profiled cooling plates *9* put on flat oval tubes *7*, whose ends are inserted and brazed into holes of lattices of tubular boxes *2* of copper M3. Water supply to tubes and security of sections are made by steel collectors *1*, brazed to tubular boxes *2* using a brazing alloy. For convenience in operation and safe service of sections in the process of manufacture the cooling plates are closed from both sides by shields *10*.

The cooling tube *7* of 1220 mm length and 19×2.2×0.55 mm section, manufactured of brass L96, serves for cooling fluid passing through it and has a contact with a cooling plate *9* and the better the contact the more effective the radiator section operation. The tube surface is deposited with a layer of brazing alloy POSSu 40-2 of 0.03–0.04 mm thickness. In brazing tubes to a cooling plate by a method of «fumigation», the layer of brazing alloy on it is not deposited preliminary. Tube ends in length 8^{+2} mm from the edge are not tin plated, as the interaction of hard and soft brazing alloy deteriorates the quality of the brazed weld [2].

Tubular box *2* of 203×153 mm dimensions represents a riveted copper structure in the form of a box with 25 mm flanging around the entire perimeter. All the ends of water-cooling pipes are grouped in the tubular box, projecting from it for $3.5^{+1.5}_{-1.0}$ mm height. The 25 mm height of the tubular box was selected so that to abut a steel collector, to eliminate all errors in assembly and to preserve 1356 mm basic size in assembly of a cooling chamber of the diesel locomotive.

Reinforcing plate *4* represents a copper plate of 3 mm thickness and 192×142 mm size. It has holes for passing a radiator tube and prevents the pool of a molten brazing alloy from flowing out from the tubular box. The reinforcing plate is also a «protective screen», preventing the heat spreading to the cooling tubes. This plate is secured to the tubular box with 20 copper rivets *3* of 0.4 mm diameter. The securing is realized in a die.

Strip *6* is a thin plate of 0.6 mm thickness and 1240 mm length, providing the rigidity of the tubular pack.

End plates *5* of 0.4 mm thickness of brass PEZ and 149×82 mm size serve for joining two semi-packs into a single unit. The end plates mounted in packs are covered by the tubular box having holes for tubes and strips. Each semi-pack is secured with four strips and two end plates.

The cooling plate *9* is a basic heat carrier in the radiator section and serves for heat dissipation into atmosphere. Number of cooling plates in a pack is 519 pieces, but this number can be changed depending on the radiator design. The plate having 151×91 mm dimensions is made from strip NDMZP (0.09×95 mm). To improve the heat dissipation into atmosphere, it has several corrugations at the surface in the form of separate stamped points. Depending on the radiator design, the design of plate can be changed. Plates are

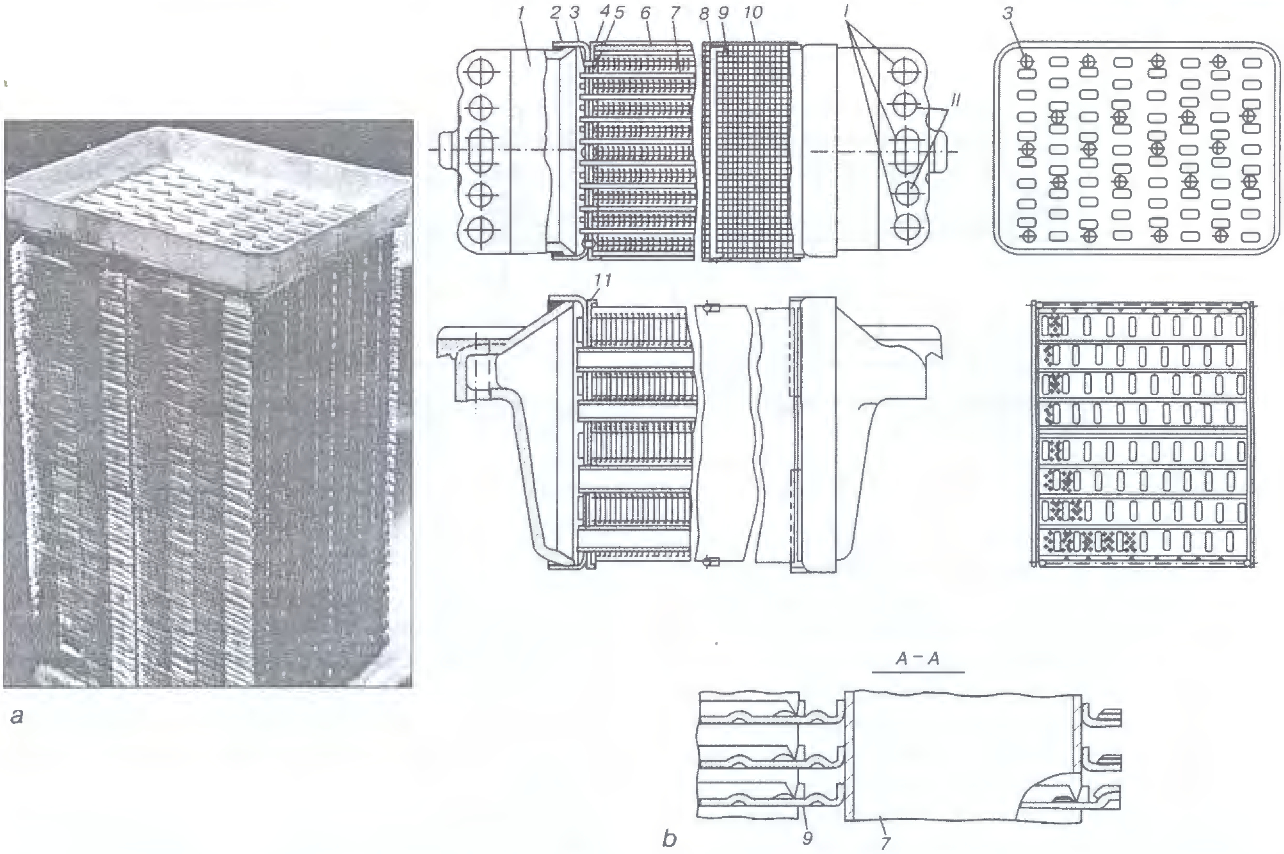

Figure 1. Appearance (*a*) and scheme of water radiator section (*b*): *1* — collector; *2* — tubular box; *3* — rivet; *4* — reinforcing plate; *5* — end plate; *6* — strip; *7* — cooling tube; *8* — rod; *9* — cooling plate; *10* — side shield; *11* — rim; *I*, *II* — holes, respectively, for water flowing and fastening of section pins to collector of a cooling chamber

manufactured in the automatic machine for assembling semi-packs of radiator sections. Holes for tubes and strips are stamped in the plate. A pitch of plates arrangement on water sections is 2.30 and 2.83 mm, while on oil sections it is 3.28 mm.

Taking into account the difficulties in technology of manufacture of radiator sections, their production is divided into three stages: sintering of a tubular pack of the section; manufacture of radiators in an assembly conveyor; inspection of sections in conveyor of a final acceptance.

Let us consider the first stage. The sintering of a tubular pack of the radiator is started at the region where the semi-packs are assembled in a specialized automatic machine (Figure 2). Cooling tubes of a definite length with a tin-plated surface and a coil of strip for manufacture of cooling plates, which is placed into the automatic machine, are fed in a special tare to the assembly area. A special cassette, in the holes of which 34 cooling tubes are fixed, is mounted in the automatic machine. After the machine switching on the plate blank is cut mechanically, stamped and the holes are punched. Then, the cooling plates with a preset pitch are put on the tubes. There are different automatic machines for assembling semi-packs (depending on the tube section). Due to this design of the automatic machines with a mechanical drive, it became possible to increase the labour productivity and to improve the conditions of the operator's work. After assembling of 519 cooling plates in tubes the semi-pack reaches 1196 mm height, then the automatic machine is switched off, and the semi-pack is removed from the cassette and packed into a

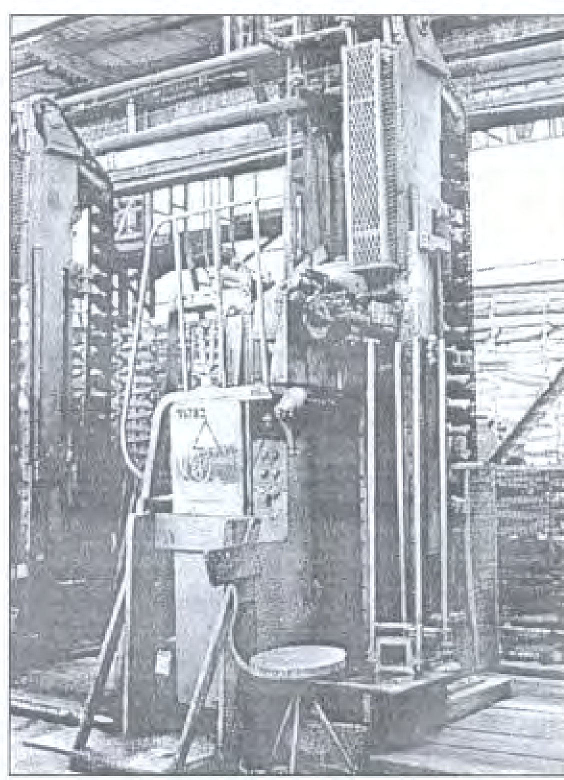

Figure 2. Automatic machine for assembly of semi-packs of radiator sections

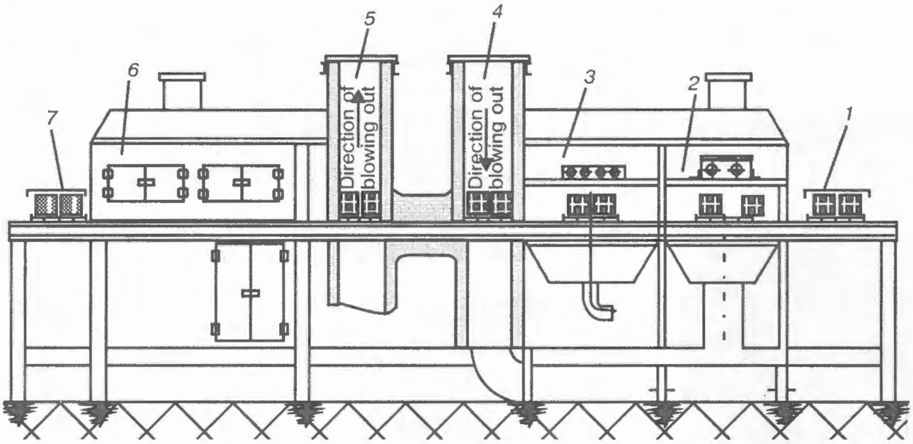

Figure 3. Schematic diagram of furnace for sintering tubular packs (existing): *1* — position of loading; *2* — chamber of fluxing; *3* — chamber of blowing out; *4* — chamber of preheating; *5* — chamber of brazing; *6* — chamber of cooling; *7* — position of unloading

special tare. The tare with semi-packs is conveyed to the area, where the tubular pack is assembled and the side shields are mounted. There are two working places at this area: assembly of the tubular pack and mounting of side shields and their fastening. At the first working place the end plates are placed on two semi-packs, and four strips are extended into holes of cooling plates to provide rigidity. Then, the semi-packs are joined by tubular boxes. After inspection by gauges of the projection of tubes from the tubular box the ends of tubes are expanded by special tools. The second place represents a specialized bench equipped with clamps and base rests for mounting of side shields and connecting cramps. The welding up of shields and cramps is made at the same bench using a shielded-gas mechanized welding. After assembly the tubular pack is packed into a special tare and conveyed to the furnace for sintering.

The mechanized gas furnace for sintering of tubular packs (Figure 3) represents an automatic line for brazing cooling plates with radiator tubes. Before the line putting into operation it is necessary to perform some preparatory operations: to fill a bath of fluxing with zinc chloride; to ignite the sintering furnace; to check the line conveyor at idle operation, and also in manual and automatic conditions; to switch on the flux feeding and to blow out the tubular packs with an air; to set the necessary temperature condition and time of holding for each technological operation; to convey two tubular packs by a telfer to the line of sintering and to place them horizontally into a cassette; to readjust the line for automatic condition.

The brazing of radiator occurs by its heating with a flow of a hot air, heated in a special chamber using gas torches. The hot air is supplied by a fan into different chambers of the furnace, where a definite temperature is created, under the action of which the brazing alloy layer on a tube is melted and the gaps are filled [3].

During sintering two packs, placed for loading into a cassette (Figure 3, position *1*), are passing automatically four chambers with 3.5 min holding in each chamber. Chambers of fluxing *2* and blowing out *3* represent a closed three-dimensional metal structure with a sprinkling unit. Solution of zinc chloride is pumped from the vessel by a centrifugal pump and fed to the system of pipelines for sprinkling. Then, the pneumatic system is switched on, which blows out the tubular packs with air. The flux remnants are flowing down to the bottom plate of the fluxing chamber and used again in the process of fluxing. After 3.5 min the packs are conveyed to the preheating chamber.

The chamber of preheating *4* has a lining for heat conservation and serves for heating tubular packs up to the temperature (220±10) °C with air, heated in separately located chambers, which is supplied to the chamber through a ventilation system.

Chamber of brazing *5* has a design, similar to the preheating chamber. Here the brazing alloy is melted at temperature (280±10) °C and fills the gaps. Then, the set of tubular packs is conveyed to the cooling chamber *6*. The tubular packs are cooled there down to temperature 80–100 °C with air blowing out using a fan. As to the design, the cooling chamber is made by the same scheme as the previous chambers. After cooling the set of radiators is removed from the sintering furnace.

In unloading (Figure 3, position *7*) the sections are removed from the cassette and mounted on a working place for inspection, where the quality of brazing cooling plates with tubes is controlled. The empty cassette is returned into initial position for a next loading. The above-mentioned control is made on both sides of external front surfaces using the method of plates displacement by a pincers in three sections, i.e. in the middle and 60 mm distance from each tubular box. In this case the plates should be strongly set on the tubes.

The automatic line of sintering tubular packs is attended by four persons, the full replacement of flux in a vessel is made four times a month, the content of iron in zinc chloride is allowed of not more than 0.07–0.08 %.

The above-described technology of sintering of radiator sections in existing furnace guarantees the required thermotechnical parameters which correspond to the technical requirements. However, in horizontal

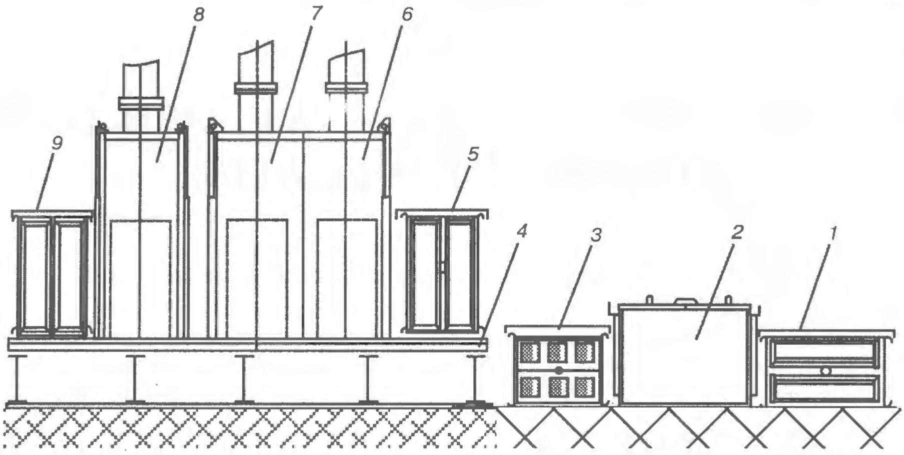

Figure 4. Schematic diagram of furnace for sintering tubular packs in vertical position: *1* — position of placing into cassettes; *2* — bath of fluxing; *3* — position of blowing out; *4* — furnace conveyor; 5 — position of loading; *6* — chamber of preheating; *7* — chamber of brazing; *8* — chamber of blowing out; *9* — position of unloading

sintering, the brazing alloy does not fill completely the gap prepared for brazing, that causes the reduction in a heat contact between the tube and cooling plate.

To reach higher thermophysical parameters and to increase the quality of manufacture of radiator sections, the specialists of HC «Luganskteplovoz» has developed a new design of the furnace for sintering packs of radiator sections, which allows brazing of sections to be performed in the vertical position, thus providing the more complete spreading of the brazing alloy and filling the gaps being brazed. It should be noted that the offered design of the furnace is developed so that to preserve the continuous passing of radiator through the whole technological cycle of the horizontal sintering furnace. Walking-beam conveyor is used as transporting means (Figure 4).

One of the specifics of the above-described furnace is the replacement of heat carriers. If in the existing furnace the air heating for preheating sections during brazing is occurred as a result of combustion of natural gas, then in this design the electrical thermal heaters are used which provide the more effective and uniform heating of the product.

The implementation of the technology of vertical sintering will increase the heat transfer of radiator section, and consequently, improve the diesel operation, resulting in increase in kilometers run of locomotives between overhauls that, in its turn, will exclude the expenses (Hr 153,000) for conductance of four scheduled annual repairs. The replacement of the natural gas for the more effective heat carrier (electric energy) will provide the economical effect of Hr 95,000. As a whole, the economical effect will amount to Hr 248,000 owing to implementation of the technology of vertical sintering of radiator sections.

1. (1985) *Diesel locomotive TE10M. Operating instructions*. Moscow: Transport.
2. Khryapin, V.E. (1981) *Handbook of tinman*. Moscow: Mashinostroenie.
3. (1984) *Handbook on brazing*. Ed. by I.E. Petrunin. Moscow: Mashinostroenie.

HEAT TREATMENT OF RAIL WELDED JOINTS IN INDUCTION UNITS

I.Z. GENKIN
All-Russia R&D Institute of Railway Transport, Moscow, Russian Federation

Results of development and application of Russian technology and equipment for welding and heat treatment of rails are presented. Introduction of the international standard "Welded Rails" is noted, the standards specifying requirements to strength, ductility and rectilinearity of the joints, and application field for rails welded by different processes.

Keywords: *flash-butt welding, gas-pressure welding, arc welding, thermit welding, heat treatment, rails*

Replacement of bolted joints by welded ones is a promising method of reinforcement of the track structure. In addition to increase of rail strength and their heat hardening, improvement of steel purity and metal quality, application of welding improves the track performance and reduces its maintenance cost.

In Russia and other countries welding is used extensively in ground railway lines, in the metro, city and industrial transport, when laying new and repairing old rails, in order to increase the rail length and move over from the jointed to continuous welded track.

Welding of rails is performed mostly by four main processes (flash-butt, gas-pressure, thermit and arc), which differ greatly by their technical and economic data. The most important characteristics in this case are the mechanical properties and consistent quality of joints, service reliability and cost of rail welding, efficiency and labour consumption of the process, mechanization and automation of work performance.

The strength and reliability of rails, welded by the flash-butt and gas-pressure processes, are determined primarily by correct selection of the technology and modes of welding, thermal and mechanical treatment of the joints, as well as strict following of these modes. In thermit and arc welding the quality of the joints and rail life depend also on the properties of filler materials.

In the railways of Russia and other CIS countries flash-butt welding is used, which provides high indices of strength and ductility of joints, the highest effectiveness and the lowest cost of work performance, mechanization and automation of the process. Welding of rail elements of the turnouts is performed by the flash-butt and thermit processes. Arc bath welding of rail elements of the turnouts is conducted. Arc bath method is used on a small scale (approximately 5 %) for welding rails in the station and tram tracks.

The work on further improvement of flash-butt technology, modes and welding machines for rail welding is performed by the All-Russia R&D Institute of Railway Transport (VNIIZhT) and Central Railway Department of the RF Ministry of Communications (RFMC), E.O. Paton Electric Welding Institute of the NAS of Ukraine, Kakhovka and Pskov Plants of Electric Welding Equipment.

Unheat-treated metal of the rail welded joints has a coarse-grained structure (Figure 1) and lower values of mechanical properties than the base metal. Metal of the joint zone, compared to that of the rolled rails, features a lower ductility, toughness and greater susceptibility to brittle fracture.

In rails of metal of a regular strength the scatter of hardness values in the welding zone falls within a narrow range (*HB* 10–30). In welding of rails of an increased and high strength a considerable loss of hardness (by *HB* 100 and *HB* 150, respectively) (see Figure 1), wear resistance and fatigue strength of metal in the head occurs in the joints.

Welding of continuous rail sections with heat and mechanical treatment of joints was developed and introduced in the railways of Russia and CIS countries to increase the strength (fatigue crack propagation time), viability, wear resistance and reliability of performance on the track.

Hardness of the head metal of welded joints of rails is increased and unified as a result of heat treatment. Metal hardness is further unified during operation in the track (Figure 1, *d, e*).

Research, conducted in VNIIZhT of RFMC, V.P. Vologdin All-Russia R&D Institute of High-Frequency Currents (VNIITVCh), Department of Tracks and Constructions of RFMC in co-operation with the rail welding enterprises, led to development of the process and equipment for welding rails of the modern and advanced modifications with differentiated heat hardening of joints and their mechanical treatment.

Differentiated heat treatment in welding of rails of the regular, increased and high strength includes bulk heating of the entire welded joint of the rails by medium-frequency currents, using special inductors and forced cooling of the head metal by air-water mixture.

Different kinds of heat treatment of the section of welded joints of rails, for instance, strengthening of the head with self-tempering, increase of metal ductility in the base and the web by normalizing, are performed as one technological operation by a preset program in the same induction equipment for different steel grades.

Grinding around the entire perimeter of joints with coarse- and fine-grained wheels was introduced to provide high fatigue strength in the head and the base, as well as in the rail web after removal of weld reinforcement by shearing or gauging and heat treatment of the joints.

Quenching of the head from welding temperatures and normalizing of the base by contact heating allow restoring the hardness and fatigue limit of the metal and provide the required ductility and brittle strength of the rails. Rails after differentiated heat treatment of joints by induction heating with medium-frequency currents have the highest values of mechanical properties of strength (breaking load) and ductility (deflection) (Table).

Brittle strength and impact toughness of the metal of welded rails rise abruptly after the local heat treatment of joints. Increase of brittle fracture resistance in welded rails of the regular, increased and higher strength improves the reliability of their operation on the track. This is particularly important in mass application of rails of new steel grades, continuous welded rail sections and rails in severe climate zones, in fast and high-speed lines.

Induction units for heat hardening of rail welded joints in the production lines of rail-welding works and on the track were developed and are manufactured in Russia.

Specification of an induction unit

Types of treated rails R75, R65, R65K, R50
Connection rail joints R75/R65, R65/R50
Power of medium-frequency current source, kV·A 250
Current frequency, kHz 2.4
Working gap between the inductor screws and rail, mm 5–10
Temperature of welded joint heating, °C 850–875
Duration of welded joint heating, s 120–240
Duration of head metal cooling (hardened rails), s:
air-water mixture 40–80
air 80–120
Duration of subcooling the head metal (not heat-hardened rails) by air-water mixture, s 10–20

Stationary units ITSM-250/2.4 include continuous-operation technological blocks, fitted with devices and instruments for conducting and documenting the process of heat treatment of rail welded joints. They also incorporate two independent matching transformers.

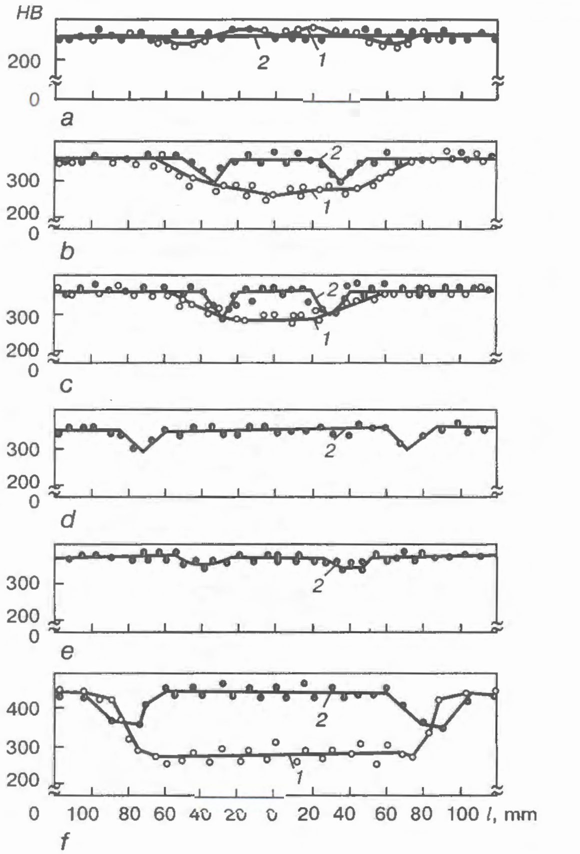

Figure 1. Hardness of the head metal in hardened welded rails of R65 type: *a–d* — of steel M76; *e* — of steel 75KhGST; *a* — not heat-hardened (small scatter of metal hardness values); *b–f* — hardened; *b, c* — welding with intermittent heating and continuous flashing, hardening from welding heat; *d, e* — hardening from induction heating with a wide and narrow heating zone in the head and welding heat (after passage of 400 mln t of gross load), during operation metal hardness in the head is further unified and increased; *f* — hardening from induction heating (significant unification and increase of metal hardness); *1* — joints without heat treatment; *2* — joints after hardening (unifying and improvement of metal hardness); circles — isolated measurements of hardness of unheat-treated welded joints (light) and after heat treatment (dark); *l* — distance from the weld

Technological blocks of the units are mounted in the flow lines after the flash-butt welding machines usually at the distance of approximately 50 m in the direction of production of welded rail sections and can move through 1–2 m in the longitudinal direction and come back, which allows the heat treatment to be performed simultaneously with welding of the subsequent joints without lowering the tempo of work

Strength and ductility of bulk-hardened welded rails of R65 type of steel deoxidized with ferroalloys with heat treatment of the joints at static transverse three-point bending

Sample, pcs	*Breaking load (numerator) and deflection (denominator)*				*Discrepancy of values*	
	Average value, kN (tf)/mm	*Main deviation, kN (tf)/mm*	*Coefficient of variation, %*	*Rejects, %*	*Evaluation criterion*	*Confidence coefficient*
16*	1929 (192.9) / 19.5	14 (1.4) / 0.8	3 / 16	– / 100	+5.4 / +5.9	1 / 1
46**	2247 (224.7) / 42	12 (1.2) / 1.3	6 / 20	–		

*Welded rails without joint heat treatment.
**Welded rails after differentiated heat treatment of the joints by induction heating.

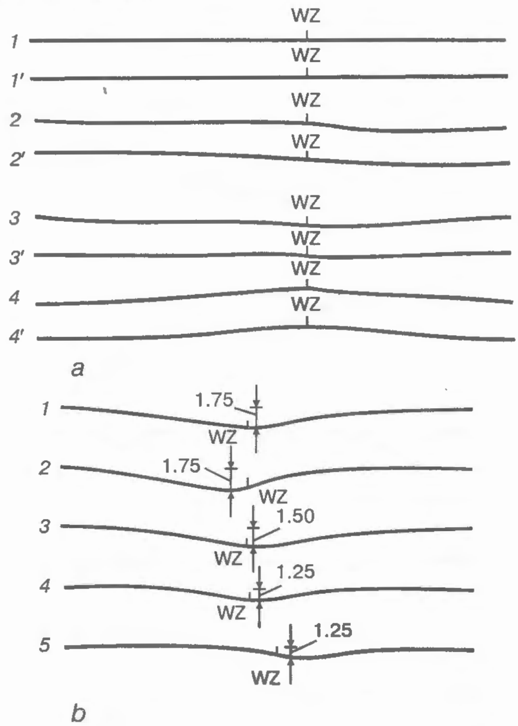

Figure 2. Longitudinal profiles of the rolling surface of hardened welded rails: *a* — local hardening of welded joints (meets specification requirements); *b* — without hardening restoration (does not meet specification requirements); *1–4* — at laying and *1′–4′* — after passage of 400 mln t of gross cargo; *1, 1′* — roughnesses within tolerance range (less than 0.3 mm per 1 m length); *2, 2′* — displacements; *3, 3′* — sagging; *4, 4′* — humps; *1–5* — sagging in welded joints after passage of 220 mln t of gross cargo over the rails, further unification and increase of metal hardness in the head occurs in operation; vertical scale 4:1; horizontal scale 1:5; WZ — welding zone

performance. Feeding and withdrawal of the rails are performed by roller conveyers of the flow lines to conduct heat treatment of the welded joints and other technological operations during section manufacture.

Field unit ITP-250/2.4 is mounted on an upgraded emergency track-repair platform. It operates as part of the complex of a mobile flash-butt welding machine for welding rails in the field, which supplies power to it. This unit includes a heating module, which carries an inductor and a sprayer. Isolating-matching transformer, capacitor banks (dehydrated, without water cooling), thyristor converter and other devices, are mounted on a platform. Power is supplied to the inductors through water-cooled cables. Hoses for air and water are fed from the platform. The water-cooling system is a closed-loop one.

The new generation units have copper inductors with iron cores. They ensure different length of heating of the welded joints in the rail head (on a small length), web and base. Application of inductors allows producing sections without sagging and achieving the required positive tolerance (humps) in the welded joints after heat treatment both in the stationary technological lines of rail-welding works and on the track.

In the Russian railways differentiated heat hardening of the joints is performed in welding of the locally-produced and imported rails primarily of the new steel grades with a high content of carbon, deoxidized with complex ferroalloys, micro- and macroalloyed with chromium, silicon and other elements.

Generalization of the research results and production experience shows, that application of differentiated heat treatment of welded joints provides restoration of the strength properties in the head metal up to the level of the base metal of the rails. The metal of the base and the web of welded rails has a fine-grained structure with high properties of ductility, toughness, time of fatigue crack propagation and survivability. All this improves the reliability, operating properties and service life of welded rails, both hardened and non heat-hardened.

Continuous welded sections and long rails, hardened with differentiated heat hardening by induction heating of the joints, have been used in the railways of Russia and CIS countries in several lines for more than 15 years, having withstood the passage of 1 bln t of gross load.

Long-term service of the rails did not reveal any formation of sagging or humps in the welded joints or connection sections at their local hardening (Figure 2).

Local heat treatment of the rails with application of new inductors does not result in development of sagging in the welds, while the available slight sagging is eliminated. This helps producing sections with an even rolling surface and positive tolerance in the welded joints in the vertical plane, which improves rail performance on the track.

Straightening of welded joints in the hot condition is applied in the rail-welding works for smoothing great sagging or crown (at local bending of not more than 2 or 3 mm on a length of 1 and 1.5 m, respectively). This allows improving the rectilinearity of welded rails, which is particularly important in connection with an increase of the velocities of train movement and wide-scale laying of continuous welded tracks.

Use of welded rails of various profiles instead of bolted joints with different coverplates is highly urgent in the tracks of the railway, as well as the city and industrial transport. This is related to the fact that such coverplates are short-lived because of stress concentration in the points of their transition from one rail to another one, particularly in fabrication under the conditions of permanent way division. Moreover, connection rails, joined by the coverplates, are the stressed portions of the track.

In this connection it became necessary to manufacture welded connection rails without disturbing their integrity and with provision of a smooth variation of the section and rigidity over the length. This was achieved by applying local heating, pressing of the base and web of large section rails to the required size, flash-butt welding of two adjacent profiles with subsequent heat and mechanical treatment of the joints.

Inductors were manufactured, which allow performing the required heating for pressing and cutting the rails mechanically with a blade tool. Mechanical treatment of welded joints, particularly connection rails, should be performed along the rail with an abrasive tool without burrs or violation of the sections, and providing smooth connections.

Joints are treated around the entire perimeter flush with the main profile along the rail with an abrasive tool with a coarse grain (125–63). In the middle part of the web on 30 mm width additional finishing is performed with an abrasive tool with fine grain (40–25) for the length of polishing of the welded joint with rotation of the wheel in the transverse direction relative to the rail.

Properly welded and treated connection rails feature a high strength and reliability of the joints, uniform quality and perform successfully under various service and climatic conditions. Transition from bolted joints with coverplates to welded connection rail extends their service life in the joint locations by ten and more times, and halves the cost.

Introduction of the developed engineering solutions on welded rails with differentiated heat treatment of the joints based on induction heating with medium-frequency currents reduces the rate of joint failure 3 times, lowers the cost for track repair and maintenance. Annual saving in the network is RUR 210 mln.

The term of guarantee of flash-butt welded rail joints is established by the amount of load, passing over them (for rails of R75 and R65 types it is 150 mln t of gross cargo, those of R50 type – 120 mln t of gross cargo).

Based on the conducted investigations and generalizations of the experience of operation in the track, VNIIZhT of RFMC and PWI of the NAS of Ukraine developed an international standard «Welded Rails» (Doc. III-1127–98). VNIIZhT of RFMC and V.P. Vologdin VNIITVCh also developed technical guidelines on welding rails and heat treatment of the joints. Welded rails with differentiated heat treatment of joints (Doc. III-1128–98) meet the requirements of the Russian specifications and the international standard. The international standard includes the developed technical requirements to the values of strength, ductility and rectilinearity of welded joints of all the typesizes and steel grades, welded by different processes, and defines the field of their application.

CONCLUSIONS

1. Technology and equipment for heat treatment of welded joints of rails have been developed and introduced.

2. Welded rails, produced locally and imported (from Austria, Canada, France, Japan, etc.) of carbon and alloyed steels, made by various welding processes with differentiated heat treatment of the joints, ensure a long service life of continuously welded sections in the track at operation under diverse service and climatic conditions.

3. An international standard «Welded Rails» has been established, which specifies the requirements to the values of strength, ductility and rectilinearity of the joints, outlines the fields of application of rails, welded by different processes.

4. Transition to heat treatment of the joints by induction heating with medium-frequency currents ensures further improvement of the quality, strength and reliability in welding continuous sections and long rails, increases the labour efficiency by 10 % and reduces the labour and material costs by 15–20 %.

PLASMA-ARC SPRAYING OF WEAR-RESISTANT COATINGS FROM COMPOSITE POWDERS FeV–B_4C

A.P. MURASHOV, Yu.S. BORISOV, L.I. ADEEVA, V.G. BOBRIK and V.L. RUPCHEV
E.O. Paton Electric Welding Institute, NASU, Kyiv, Ukraine

The process of plasma spraying, structure and properties of coatings from composite powders «ferrovanadium–boron carbide» are considered. Analysis of phase composition of the coatings and powder particles that have passed through the plasma jet shows that reaction of exothermic interaction of components to form vanadium and iron borides and carbides takes place during the spraying process. Microhardness of the coatings amounts to 16,930–18,920 MPa.

Keywords: *plasma-arc spraying, composite powders, ferrovanadium, boron carbide, synthesis, phases, exothermic reaction, dispersed-strengthened structure*

Increase in wear resistance of machine units or parts operating under conditions of abrasive impact of a working environment can be achieved through applying wear-resistant thermal spray coatings. Wear-resistant coatings from powders containing tungsten, titanium and chromium carbides (Amperite-502, Metco-439, Metco-31S etc.) as a reinforcing phase, or glazed Ni–Cr–Si coatings containing reinforcing phases in the form of boride and carbide compounds are applied to air-ducts, components of fans, pumps, moulds and dies to manufacture parts from metallic, ceramic and polymeric materials or glass [1].

This study considers the processes of deposition of coatings by the plasma-arc spraying method using composite powders consisting of ferrovanadium and commercial boron carbide. The choice of this material is based on the fact that, in addition to availability of its components, when heated it can form iron carbides and borides, and particularly vanadium carbides and borides which are not inferior to tungsten carbide in their performance [2]. The use of the chosen composition for spraying of coatings is of interest also because of heat released due to exothermic reactions taking place during formation of new phases, which is favourable for formation of wear-resistant plasma coatings.

Conglomerated powder produced by using a polyvinyl alcohol as a binder was employed for spraying. In addition, the use was also made of a powder produced by partial sintering of briquettes compacted from a mechanical mixture of the ferrovanadium and commercial boron carbide powders subjected subsequently to crushing, grinding and separation of particles of not less than 100 μm in size. In both cases the ratio of weight of ferrovanadium to that of boron carbide was 5:1.

Plasma-arc spraying of coatings was performed using the versatile plasma unit UPU-8M equipped with a plasmatron operating with the argon-nitrogen plasma gas mixture. A special extension nozzle was employed to limit the access of oxygen to the spray material during the spraying process. Spraying was carried out by the two methods: with and without the extension nozzle. Coatings were deposited on samples of steel St3 measuring 15×20×3 mm, thickness of a coating being not less than 0.35 mm. At the same time, a material was water atomised, followed by entrapping of the atomised particles. The spraying parameters were identified after optimisation on coatings produced from a composite thermal-sensitive powder 80 % Ni–20 % Al with a particle size of 60–100 μm chosen as a model material. The following parameters were selected: I_w = 450 A; U_w = 55 V; plasma gas flow rate, l/min: argon — 34, nitrogen — 12; spraying distance — 140 mm. In the case of using the extension nozzle, the latter was 200 mm. Examination of structure and phase composition of powders and coatings was done by metallography and X-ray diffraction phase analysis.

Examination of phase composition of initial powders showed that the conglomerated powder consisted of raw components with an insignificant content of $V_4C_{2.67}$ and traces of $B_{13}C_2$, B_8C and V_3O_4 (Table). The preliminarily sintered powder contained, in addition to the raw components, also V_3B_4, V_2B_3, σ-FeV, FeV_4O_4, V_6C_7 and V_3O_4, which is indicative of the formation of new phases during the sintering process.

Differential thermal analysis (DTA) of samples compacted from the conglomerated powder allowed a conclusion that an exothermic reaction was initiated at a temperature of 940–1180 °C to form new phases with a substantial increase in temperature. X-ray diffraction phase analysis made it possible to identify these phases as vanadium borides of the V_3B_4 and V_2B_3 types. In addition to these phases, also VB, Fe_2B and carbides V_2C and Fe_3C were detected. The DTA data proved the possibility of formation of new phases in plasma spraying of coatings from powders of the FeV–B_4C system with the exothermic effect.

Substantial increase in luminescence of the plasma jet, characteristic of the spraying process involving thermal-sensitive powders, was seen during the spraying process, the increase in luminescence of the jet

Results of X-ray diffraction phase analysis of coatings and powders of the FeV–B_4C system

Material analysed	*Conglomerated powder*	*Sintered powder*	*Sintered powder + NiAl powder*	*After DTA*
Initial powder	FeV, B_4C, σ-FeV, $V_4C_{2.67}$, $B_{13}C_2$, B_8C (traces), V_3O_4	FeV, V_3B_4, V_2B_3, σ-VFe, FeV_4O_4, B_4C, V_6C_7, V_3O_4	FeV, V_3B_4, V_2B_3, σ-FeV, FeV_4O_4, B_4C, V_6C_7, V_3O_4, Ni, Al, γ-Al_2O_3 (traces)	V_3B_4, V_2B_3, V_2C, VB, V_5B_6, Fe_2B, Fe_3C, FeV (traces), B_4C
Entrapped powder	FeV, VB, B_4C, VC, V_3O_4, V_5B_6, V_2C, σ-FeV, V_8C	Fe_2B, V_5B_6, FeC, σ-VFe, FeV, B_4C (traces), V_3O_4, Fe_3O_4	–	–
Coating:				
without extension nozzle	FeV, VB, VC, V_3O_4, V_8O_5, V_2C, σ-FeV, Fe_2O_3 (traces), Fe_3O_4	Fe_2B, V_5B_6, FeC, σ-FeV, FeV, B_4C (traces), V_3O_4, Fe_2O_3	V_5B_6, $Fe_{23}(C, B)_6$, σ-FeV, Fe_3C, γ-Al_2O_3, Ni_3Al	–
with extension nozzle	FeV, V_5B_6, VB, σ-FeV, V_2C, V_3B_2, V_8O_5, Fe_2O_3 (traces)	Fe_2B, V_5B_6, FeC, σ-FeV, FeV, B_4C (traces), Fe_2O_3	V_5B_6, $Fe_{23}(C, B)_6$, Fe_2C, σ-VFe, γ-Al_2O_3, V_3B_2, Ni_3Al	–

being much more intensive in the case of using the conglomerated powder.

Atomisation of powder particles into water made it possible to determine that they had an oval shape, close to the spherical one. Structure of such particles is of the dispersed-strengthened type. Moreover, particles of a fragmented shape characteristic of B_4C (Figure 1) were also seen. Examination of phase composition showed the presence of FeV, V_5B_6, VB, σ-FeV, B_4C, V_2C, V_3B_2 and V_8O_5, as well as traces of Fe_2O_3, Fe_3O_4 (see the Table) in this powder.

The above results evidence a complete melting of particles of the composite powder in the plasma jet and exothermic reactions of formation of carbide and boride compounds taking place under such conditions. The presence of the FeV and B_4C particles in a composition of the entrapped powder is attributable to isolated unbounded particles of ferrovanadium and boron carbide present in the composite powder.

Examination of structure of the coatings produced from the conglomerated powder showed that they were formed from molten particles in the form of lamellae. A coating comprises light and dark-grey zones. Etching of the coating in a mixture of aqueous solutions of nitric and fluoric acids revealed a multiple-phase nature of its structure. The light zones in the form of lamellae correspond to FeV, and the dark-grey ones are a finely dispersed structure (Figure 2). Oxides are present in insignificant amounts in the form of thin grey films on boundaries of the particles.

Compared with phase composition of the powder, the coatings had such new phases as VB, VC, V_3O_4, V_8O_5 and V_5B_6, as well as a small amount of V_2C and σ-FeV. Particles that have a heterogeneous structure consist of a ferrovanadium matrix and reinforcing carbide and boride inclusions uniformly distributed in it.

Coatings sprayed from powders produced by preliminary sintering contain a small amount of pores and have uniformly distributed light and dark zones. Traces of oxides in the form of thin grey films on the boundaries of a number of particles were seen in their structure (like in the coatings produced from the conglomerated powders). A finely dispersed heterogeneous structure containing dark small particles was revealed in the light zones by etching. The dark zones are susceptible to spalling during treatment. Suppos-

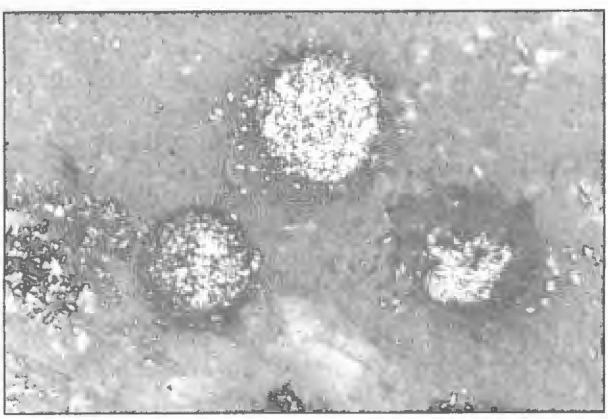

Figure 1. Microstructure of particles that passed through the plasma jet and were entrapped in water (×500)

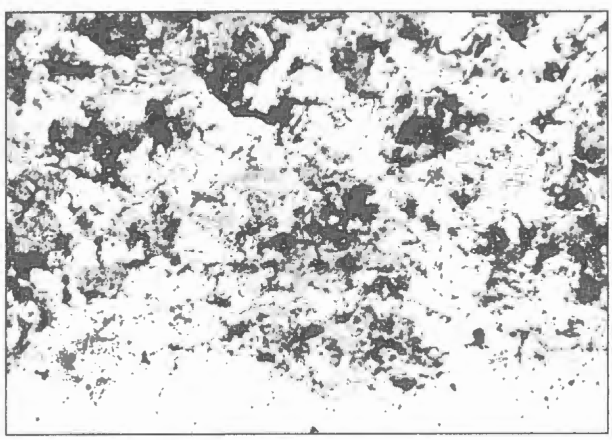

Figure 2. Microstructure of coatings produced from conglomerated powder FeV–20 % B_4C by using an extension nozzle (×500)

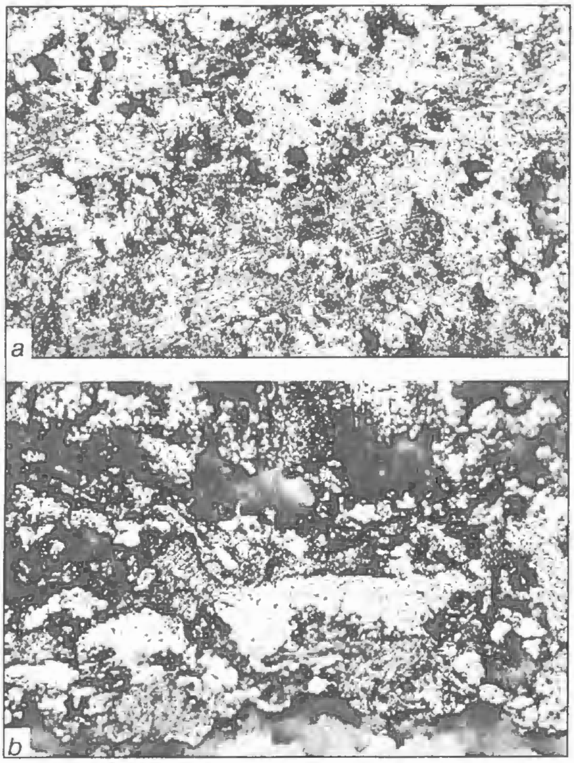

Figure 3. Microstructure of coatings produced from powders FeV–20 % B_4C + 50 % NiAl: *a* — without extension nozzle (×800); *b* — with extension nozzle (×500)

edly, they are boron carbide particles that did not participate in synthesis of the new phases.

Differences were detected between phase compositions of coatings and a powder containing vanadium borides and carbides synthesised during the process of production of the powder using sintering. Unlike the powder, the coatings had new phases, such as F_2B, V_5B_6 and FeC. In addition, they contained much less oxides (see the Table).

Maximum microhardness of the coatings produced from the conglomerated powder and powder made by preliminary sintering was 13,710–16,930 MPa. Microhardness of the light zones corresponding to FeV was 2710–3200 MPa. The use of an extension nozzle made it possible to produce coatings with a lower content of oxides.

Powder in the form of a mechanical mixture (1:1 in weight) of a thermal-sensitive powder Ni–20 % Al and powder FeV–20 % B_4C, produced by sintering, was prepared to provide coatings with an increased content of a metal binder. Coatings deposited from this mixture have low porosity and strongly adhere to the substrate. They have a heterogeneous structure and a large light zone (Figure 3). Etching reveals a dispersed-strengthened structure in such zones. Microhardness of these zones is 12,970–18,920 MPa. In the case of using an extension nozzle, the uniformity of distribution of light and dark zones is lower. Light-grey regions characteristic of intermetallics NiAl are seen in the coatings. The phases that prevail in the coatings are V_5B_6 and $Fe_{23}(C, B)_6$.

CONCLUSIONS

1. Processes of plasma spraying of coatings using composite powders FeV–B_4C were studied. It was found that during plasma-arc spraying the formation of new phases accompanied by release of heat of exothermal reactions takes place already in the plasma jet. Coatings formed under such conditions comprise carbide, boride and a small amount of oxide compounds of iron and vanadium. The presence of oxides in the coatings is attributable to the oxidation processes, as well as to their presence in an initial powder.

2. Application of an extra extension nozzle leads to decrease in the amount of oxides in the coatings, and provides a wide range of phase composition with regard to the content of vanadium borides. The sprayed coatings have a heterogeneous structure consisting of a ferrovanadium matrix and inclusions of vanadium borides having a microhardness of about 19,000 MPa. The presence of a tough substrate and a strong reinforcing phase characterised by high hardness is a favourable combination leading to increase in abrasive wear resistance of the coatings.

1. Borisov, Yu.S., Kharlamov, B.A., Sidorenko, S.A. et al. (1987) *Thermal coatings from powder materials*. Kyiv: Naukova Dumka.
2. (1976) *Properties of elements*. Refer. Book. Part 1. Physical properties. Ed. by G.V. Samsonov. Moscow: Metallurgiya.